Politecnico di Torino

Master Degree in Nanotechnologies for ICTs

Master Degree Thesis

Energy harvesting from low-grade heat through supercapacitors

Supervisor

Prof. Andrea LAMBERTI

Co-supervisor

Dott. Pietro ZACCAGNINI

Candidate

Mario GEMMA

December 2023

A Carmen,
la sola al mondo che sa, del mio cuore,
ciò che è stato sempre, prima d’ogni altro amore.

Summary

Climate change is the defining issue of our time. The current energy system is not sustainable and major transitions are needed. In 2021, The International Energy Agency (IEA) reported that over 60% of the total primary energy demand was wasted as heat [8]. Studies have estimated that 63% of this waste heat is low-grade thermal energy, i.e., at a temperature below 100 °C [7]. Improving energy efficiency by focusing on waste heat recovery is widely recognized as a crucial tool to mitigate the increasing global energy demands and reduce GHG emissions. Low-grade thermal energy harvesting poses significant challenges to traditional thermoelectric systems. This thesis work reports the implementation and analysis of a method for the conversion of low-grade heat into energy. It is based on a thermocapacitive cycle involving charging, heating, discharging, and cooling within a temperature range of 0°C to 80°C through the use of a supercapacitor. A voltage output is recovered after every cycle. Unlike previous methods, this technique does not require a fixed temperature gradient. Instead, it operates in a homogeneously changing temperature. It relies on the temperature dependence of the cell voltage of a charged supercapacitor. The mechanism is attributed to potential variation due to thermal energy variation at both electrodes. This study carries out a systematic investigation of supercapacitors comprising activated carbon based electrodes and different electrolytes, namely the ionic liquid [PYR14] [TFSI], the organic salts TEA BF4 and TEA TFSI in propylene carbonate. In order to understand the role of each component of the device and to improve the overall performance of the manufactured device as well as the extractable power, several characterizations have been performed: electrolyte characterization such as conductivity and viscosity measurements; electrochemical characterization of supercapacitors. In conclusion, the high tunability of the system proposed makes it very promising to low-grade thermal energy harvesting research, due to the implementation of sustainable materials and cost-attractive technologies.

Table of Contents

1. Energy system 1
- 1.1 The energy system and the climate change 1
- 1.2 Energy harvesting 3
- 1.3 Global waste heat potential estimation 4
- 1.4 Thermal energy harvesting: a perspective 6

2. State of the art 8
- 2.1 The evolution of heat to electricity 8
  - 2.1.1 Heat engines 8
  - 2.1.2 Thermoelectric energy harvesting 8
- 2.2 Beyond Thermoelectrics 11
  - 2.2.1 Pyroelectric energy harvesting 11
- 2.3 Electrochemical thermal energy harvesting 13
  - 2.3.1 Thermogalvanic Cells 13
  - 2.3.2 Thermally regenerative electrochemical cycle systems 14

3 Supercapacitors 17
- 3.1 Electrical Double Layer 18
- 3.2 Electrical Double Layer Capacitors 19
- 3.3 Electrical Double Layer Capacitors electrolytes 21
- 3.4 Supercapacitors for thermal energy harvesting 22

4 Materials and Methods 26
- 4.1 Performance evaluation parameters 26
  - 4.1.1 Specific capacitance 26
  - 4.1.2 Coulombic and energy efficiency 26
  - 4.1.3 Equivalent series resistance 27
- 4.2 Characterization methods 27
  - 4.2.1 Conductivity measurement 27
  - 4.2.2 Viscosity measurement 28
  - 4.2.3 Electrochemical characterization methods 29
- 4.3 Fabrication steps and experimental setup 31

5 Results 35
5.1 Electrolytes characterization 35
5.1.1 Ionic conductivity 35
5.1.2 Viscosity 38
5.1.3 Walden plot 39
5.2 Electrochemical EDLCs characterization 40
5.2.1 Leakage current and self-discharge 41
5.3 EDLC thermal energy harvesting 48

6 Conclusions and future developments 53

7 Bibliography 57

Chapter 1

Energy system

This introductory chapter provides an overview and brief analysis of the global energy system and its critical issues. The upcoming section will examine the potential impact of energy harvesting in this context, with specific focus on thermal energy harvesting. An overview of the estimated global waste heat potential will also be provided.

This chapter emphasizes the need to consider not only the technical aspects but also the social context that this research is part of, in order to underline the multidisciplinary nature of the subject.

1.1 The energy system and the climate change

Climate change is the defining issue of our time and we are currently facing a critical and dramatic moment. The impacts of global warming are global in scope and unprecedented in scale. Widespread and rapid changes in the atmosphere, ocean, cryosphere and biosphere have occurred and the global implications range from shifting weather pattern (that threaten food production) to rising sea levels (that increase the risk of destructive flooding). The susceptibility of ecosystems and individuals to climate change varies considerably among and within regions. Approximately 3.3 to 3.6 billion people live in contexts that are highly vulnerable to climate change. According to the Intergovernmental Panel on Climate Change (IPCC) Sixth Assessment Report (AR6), it is "unequivocal that human influence has warmed the atmosphere, ocean and land” since pre-industrial times [1]. Without drastic actions today, adapting to these impacts will be more difficult and costly in the future. To enhance global response to the menace of climate change 196 parties signed the Paris Agreement at the 2015 United Nations Climate Change Conference. Its main aim is to hold “the increase in the global average temperature to well below 2°C above pre-industrial levels” and pursue efforts “to limit the temperature increase to 1.5°C above pre-industrial levels.” [2]. The anthropogenic activity with the greatest impact on climate change is related to the emission of greenhouse gases (GHG), especially CO_2, and the trend is increasing over the years, as shown in Figure 1.1.

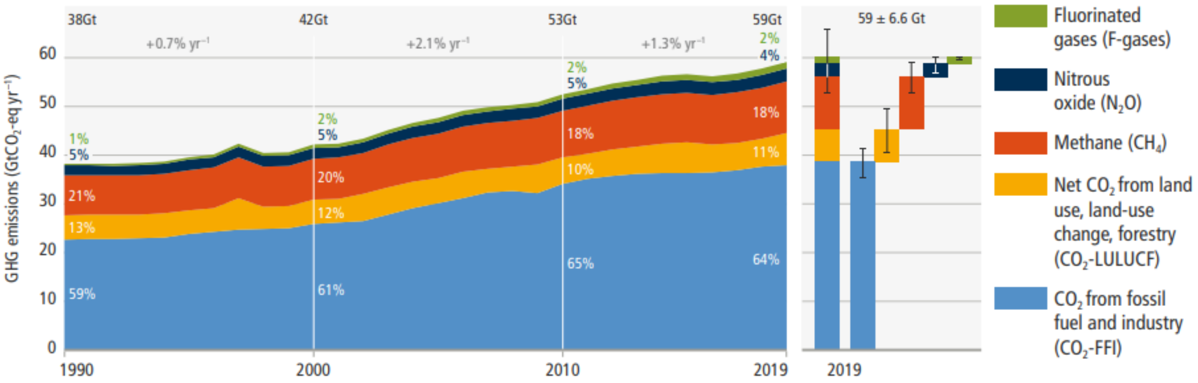

Figure 1.1: Global net anthropogenic GHG emissions (in $GtCO_2$-eq yr^{-1}) 1990–2019 [3].

Figure 1.2 shows that the sector contributing most to GHG emissions is the energy sector.

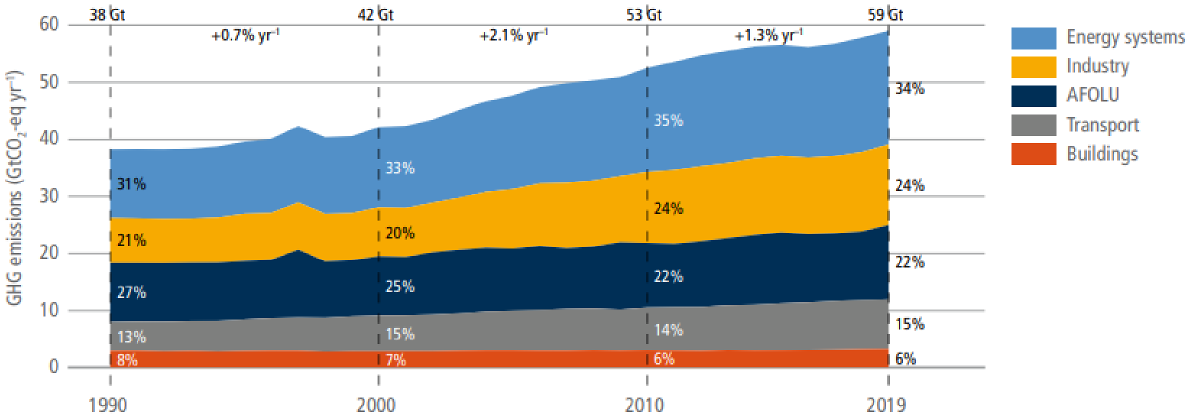

Figure 1.2: Global anthropogenic GHG emissions (in $GtCO_2$-eq yr^{-1}) by major economic sector [4].

Reducing emissions poses a challenge in light of the constantly growing demand for energy, as can be seen in figure 1.3, where the total energy supply refers to the overall supply of energy for all activity within a country's territory. It comprises energy requirements for energy transformation, support operations of the energy sector itself, transmission and distribution losses, final energy consumption (such as for industry, transport, households, services, agriculture), and the utilization of fossil fuel products for non-energy related purposes. In 2019, just 13.8% of the global total primary energy supply (TPES) originated from renewable energy sources, which includes hydro, biofuels, renewable municipal waste, solar PV, solar thermal, wind, geothermal and tidal.

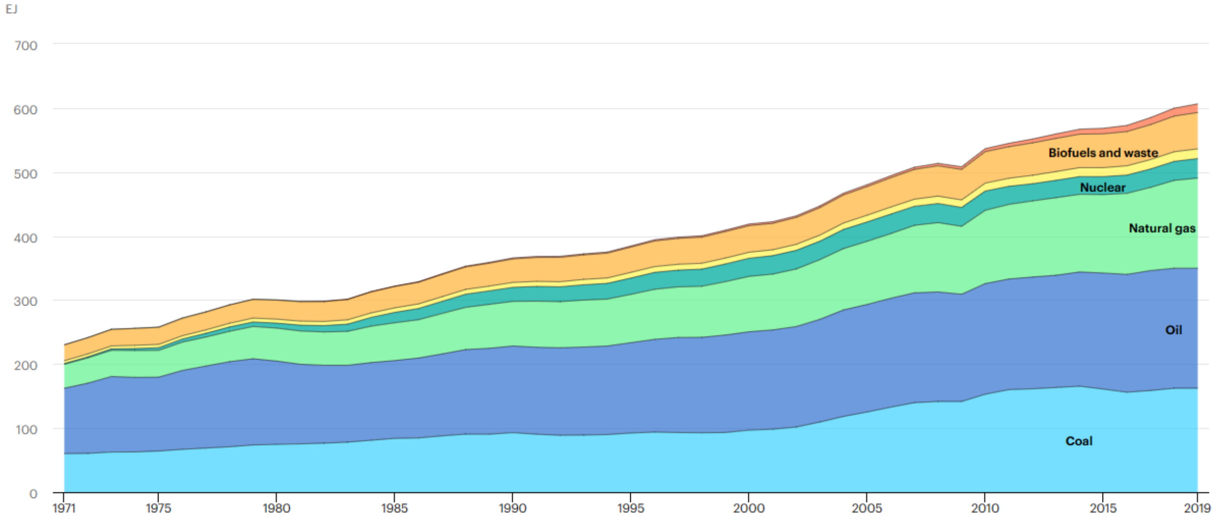

Figure 1.3: World total energy supply by source, 1971-2019 [5].

In conclusion, the current energy system is unsustainable and major transitions towards an energy-sustainable economy and society are needed to reduce GHG emissions throughout the whole energy sector. This will involve significantly decreasing the overall use of fossil fuels, deploying low-emission energy sources, switching to alternative energy carriers, improving energy efficiency and conservation.

1.2 Energy harvesting

In the context of pursuing a sustainable transition, harvesting assumes a crucial role. Energy harvesting is the process of converting an otherwise wasted amount of energy into electricity and storing it for later use. Among the sources of energy that can be exploited are solar energy, thermal energy, wind energy, salinity gradients and kinetic energy. There has been a rise in interest in energy harvesting in recent years, as evidenced by the increase in the number of publications about energy harvesting (figure 1.4). This is due to a greater sense of responsibility towards energy and the environment, as well as a rising demand for energy due to recent digital trends, such as Internet of Things (IoT) devices. The global energy harvesting market by technology is shown in figure 1.5, highlighting that the thermoelectric sector has been the largest in 2014.

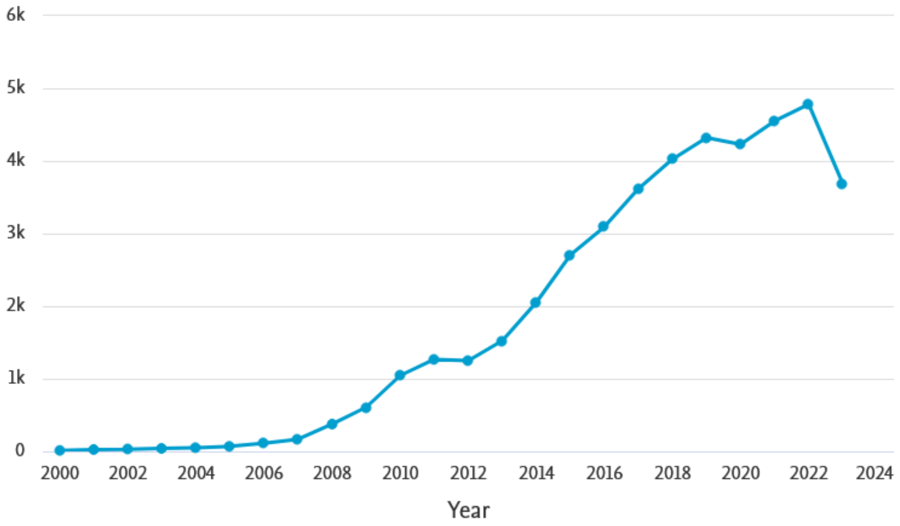

Figure 1.4: Number of publication in the field of energy harvesting from 2000 to 2023, from Scopus.

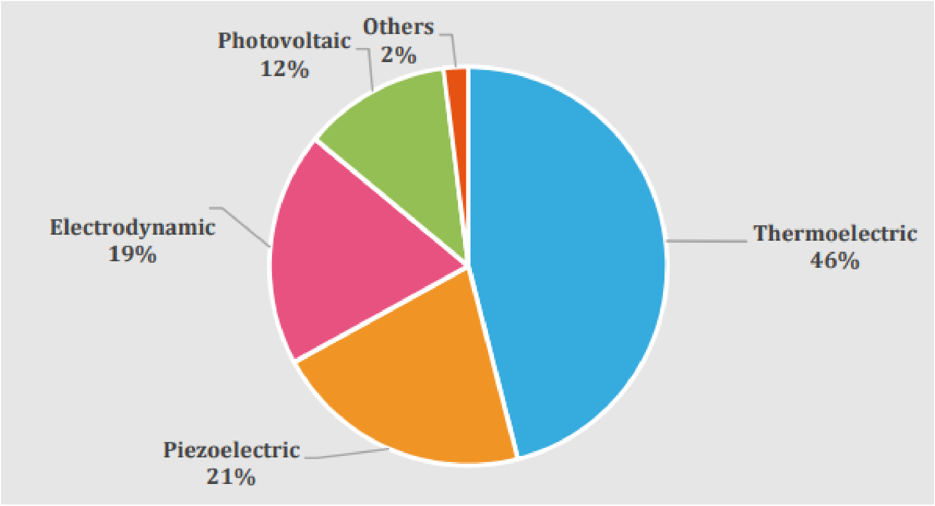

Figure 1.5: Global energy harvesting market by technology in 2014 [6].

1.3 Global waste heat potential estimation

Energy efficiency is widely recognized as a crucial tool to mitigate the increasing global energy demands and reduce GHG emissions. The process chain of energy conversion from primary energy sources to final energy use is affected by several losses. In end use in particular, a significant portion of converted energy is produced as waste heat, which typically dissipates into the environment. This waste heat needs to be recovered for specific purposes to increase process efficiency. Yet the challenge is that it can occur in a variety of ways and situations that determine its usability. Factors such as uninterrupted or intermittent availability, temperature ranges, the mode of thermal transfer (radiation, convection or conduction), and the configuration and composition in case of fluids, as well as the location between source and sink, are all crucial considerations. The IEA reported that the global energy supply in 2021 has been about 624 EJ (10^{18} J) and for an initial estimation, over 60% of the global energy demand has been wasted as heat, as can be seen in figure 1.6.

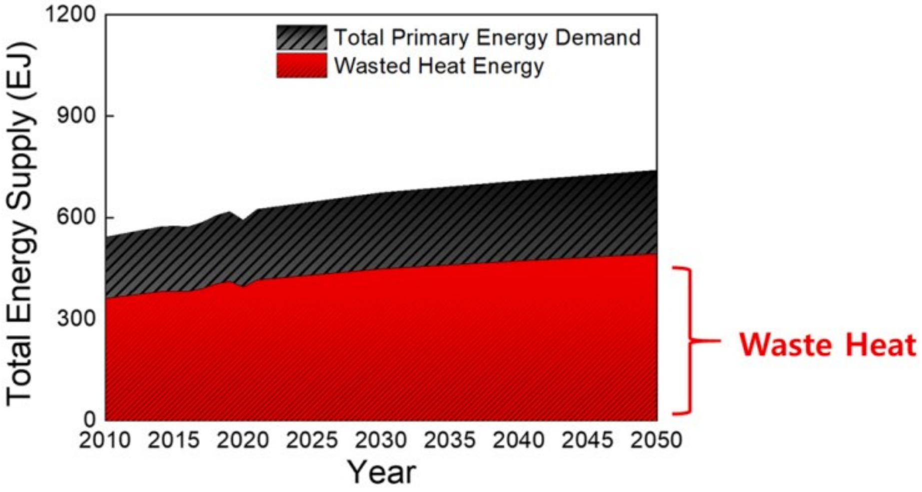

Figure 1.6: Global primary energy demand trends projected to the year 2050 and the portion of waste heat in total energy use [8].

Several studies have been conducted to estimate the amount of the available resource. The work of Formann et al. [7] proposes an approach, based on conversion efficiencies, to estimate the waste heat potential of the four most common sectors of end use (transportation, industrial, commercial and residential) as well as the electricity generation on a global scale. According to this study, each of these five sectors has been associated with an end-use efficiency. The estimation accounts for various temperature ranges of waste heat. In this top-down approach, the focus is on the input side of conversion processes downstream to final energy consumption. For the global energy flow estimations, IEA data from 2012 are used. After separating all flows into energy service and rejected energy, it emerges that about 72% of the global energy input is lost after conversion (fig. 1.9). Figure 1.7 shows that the largest proportion of wasted heat comes from electricity generation (39% of globally rejected energy), in the form of low temperature waste heat (i.e. < 100°C).

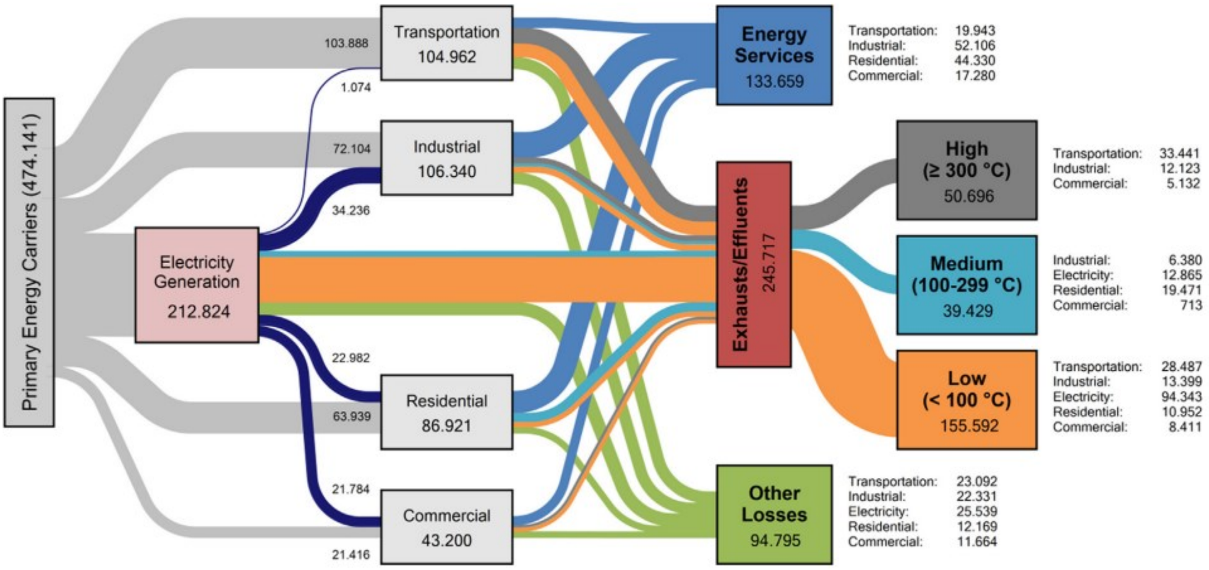

Figure 1.7: Estimated global waste heat distribution of 2012 in PJ (according to Formann et al. theoretical approach) [7].

This study offers an analysis of waste heat distribution based on temperature, presenting sectoral shares (fig. 1.8). Note that these shares focus only on the exhausts/effluents fraction (fig.1.9), with waste heat temperatures for exhausts and effluents categorized into ranges below 100 °C, between 100 and 299 °C, and 300 °C or above.

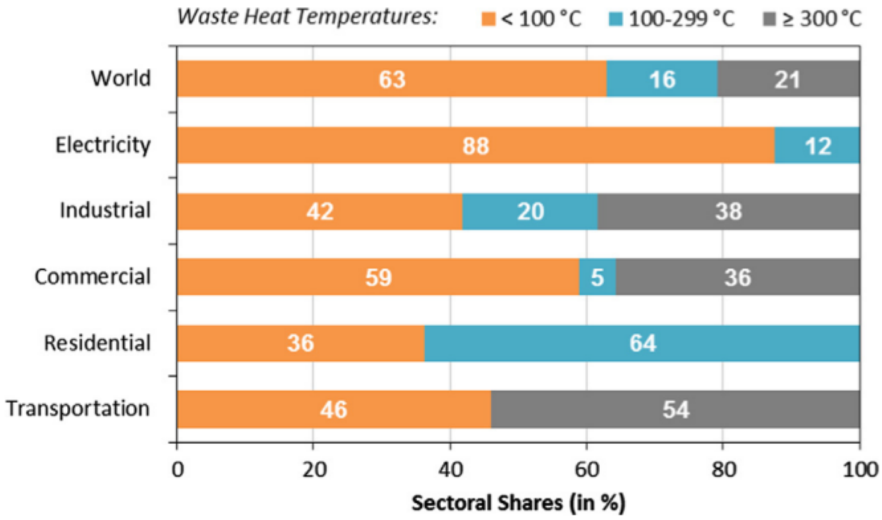

Figure 1.8: Sectoral shares of waste heat distribution.

In summary, 63% of the waste heat streams considered occur at a temperature below 100°C, with electricity generation being the largest contributor, followed by transport and industry.

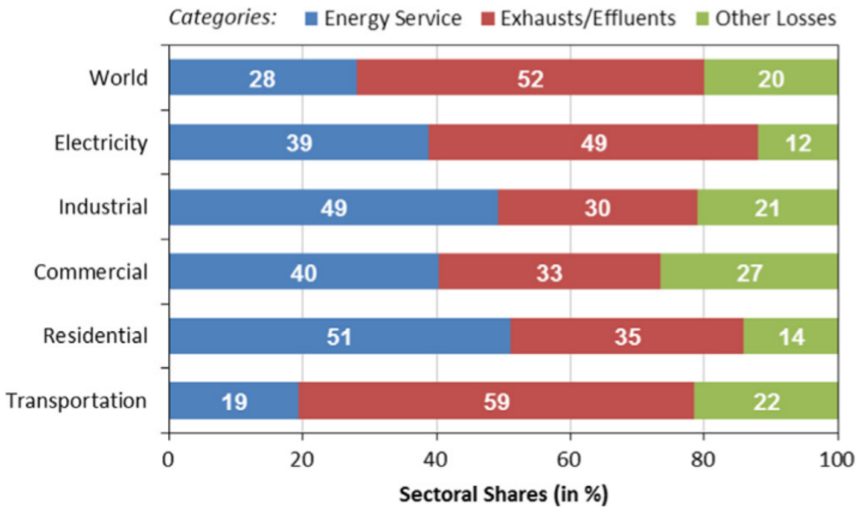

Figure 1.9: Sectoral shares of balance factors.

All sectors, particularly the commercial sector, exhibit a relatively high quantity of low-temperature waste heat (below 100°C). In the residential and electricity generation sectors, there is no high-temperature waste heat (300 °C) and no medium-temperature waste heat (100-299 °C) in the transportation sector.

Another work worth citing is the more recent study by Firth et al. [9]. Their research spans several years and various scenarios, whereas Froman et al.'s work is limited to the year 2014. However, the results are comparable in all sectors and overall.

Thus far, waste heat has only been quantitatively evaluated. However, an investigation into the quality of the rejected energy is necessary to determine its practical applications.

1.4 Thermal energy harvesting: a perspective

According to what has been said so far, waste heat can be classified into three classes: high temperature (above 300 ◦C), medium temperature (100-299 ◦C) and low temperature (below 100 ◦C). High- and medium-grade waste heat can be effectively recovered, as it is present close to power plants. Furthermore, the thermal cycle efficiency, determined by the difference in temperature between the heat source and sink, proves profitable at elevated temperatures. Therefore, multiple methods have been developed and employed in the medium to high-temperature range. On the other hand low-grade waste heat is often ignored due to its inefficient conversion (compared to medium and high grade waste heat) and difficulty of recovery as the heat source is more widespread and less concentrated than higher temperature waste heat. Further exploration of low-grade waste heat recovery is necessary due to its significant potential for recovering energy, exceeding that of both medium and high-grade waste heat combined. A practical method of exploiting such a source could revolutionize global energy demand issues. Solid-state thermal energy harvesting devices are highly regarded as one of the most promising technologies because of their potential to be located near end-use sites (heat sources). They require minimal operational costs and space, making them an attractive option [8,10]. These devices operate by using different technologies like thermoelectric, pyroelectric, thermomagnetic, and thermionic.

Chapter 2

State of the art

This chapter will focus on technology. Firstly, a short summary of the various methods used to convert heat into electricity will be provided. In a subsequent part, it will be examined the electrochemical thermal energy harvesting technology in greater detail to establish the context for this work.

2.1 The evolution of heat to electricity

2.1.1 Heat engines

A heat engine is the most common way of converting heat into electricity. It works through a thermodynamic cycle that converts heat into usable energy that can be used for mechanical work. This is basically done by bringing a working substance (fluid) from a higher state temperature T_H (source) to a lower state temperature T_L (sink). The T_H and T_L values determine the Carnot efficiency i.e., the maximum energy conversion efficiency of the heat engine, which is defined as:

$$\eta_c = 1 - \frac{T_L}{T_H}$$

More direct methods of converting heat into electrical current exist. Among the low-grade thermal energy harvesting technologies, the most promising ones currently rely on the thermoelectric, pyroelectric, thermomagnetic, thermoelastic and electrochemical effects [8,10].

2.1.2 Thermoelectric energy harvesting

Thermoelectric energy harvesting is the most popular and studied of the low-grade thermal energy harvesting technologies. Thermoelectric engines operate between two heat reservoirs that have different temperatures (like a heat engine), but they are based on different physical concepts. The term Thermoelectric (TE) effect comprises three separately identified effects: the Seebeck effect, the Peltier effect, and the Thomson effect. The Seebeck and Peltier effects are distinct manifestations of the same physical process, hence it is commonly known as the Peltier-Seebeck effect. Another phenomenon that can be considered, and is not typically referred to as a thermoelectric effect, is Joule heating: the heat that is produced when an electric current flows through an electrical conductor. The remaining effects will be discussed in the following sections.

Seebeck effect

The Seebeck effect refers to the electromotive force (emf) that arises between two points of an electrically conductive material when there is a temperature difference between them. This induced voltage is kwon as Seebeck emf and it is directly proportional to the temperature difference. The Seebeck coefficient S_C is defined as:

$$S_C = \frac{V_{out}}{\Delta T}$$

where V_{out} is the induced voltage and ΔT is the temperature difference. Semiconductor materials have higher S_C values (greater than 100uV/K) when compared to metals. This is the reason why they are widely used in thermoelectric modules. Seebeck effect can be explained as follows: electrons on the hot side, which gain kinetic energy proportional to the increase in temperature, move towards the cold side, creating a difference in electron density until an electric field is established to prevent further electron flow, thus achieving an equilibrium in charge density. When two distinct conductors are connected together, and their respective junctions are placed along a temperature gradient, due to the inherent difference in electron energies in the two materials, the electron energy levels in each conductor will shift differently, creating a voltage difference between the junctions.

Peltier effect

The Peltier effect represents the reverse of the Seebeck effect: when an electric current flows through the junction of two thermoelectric (TE) materials, the Peltier effect results in cooling or heating at that junction. The Peltier heat is directly proportional to the electric current in the circuit, but its sign (cooling or heating) depends on the direction of the current. The magnitude of Peltier heat is provided as follows:

$$q = (\pi_a - \pi_b)I$$

where I is the electric current flowing from material a to b, and π_a, π_b are the Peltier coefficient for the respective materials.

Thomson effect

The Thomson effect arises in a thermoelectric material that is not uniformly heated. In the case of most thermoelectric materials, the Seebeck coefficient is temperature dependent. Therefore, when there is a spatial temperature gradient in these materials and a current flows through them, a continuous version of the Seebeck and Peltier effects takes place, resulting in Thomson heat. The heating rate per unit length of the conductor is directly proportional to the electric current I and temperature gradient, and is defined as:

$$\frac{dq}{ds} = \tau I \frac{dT}{ds}$$

where τ is the Thomson coefficient.

Thermoelectric generator

A thermoelectric generator (TEG) is a solid-state device that exploits the Seebeck effect to convert heat directly into electrical energy. It operates when exposed to a heat source of higher temperature on one side and a heat sink of lower temperature on the other. Figure 2.1 shows the main components of a TEG module. The fundamental element of a TEG is the thermocouple, which consists of a p-type and an n-type semiconductor. These materials are electrically connected in series and thermally connected in parallel, commonly forming a pi-shaped structure. The operation of the thermocouple in power generation mode is depicted on the left-hand side of Figure 2.1. The thermocouple is connected to an external circuit and a thermal gradient is applied across both sides. As a result, a current flows in the external circuit from the p-type to the n-type semiconductor. A TEG module comprises numerous thermocouples, which are electrically connected using metal electrodes. To prevent inter-diffusion between thermoelectric materials and electrodes and to reduce contact resistance, it is common practice to use diffusion barrier layers made from Ti, Mo, or Ni at the interface. Additionally, the arrays of thermocouples are placed between thin ceramic substrates such as Al_2O_3 (alumina) and AlN (aluminum nitride) to electrically insulate the system.

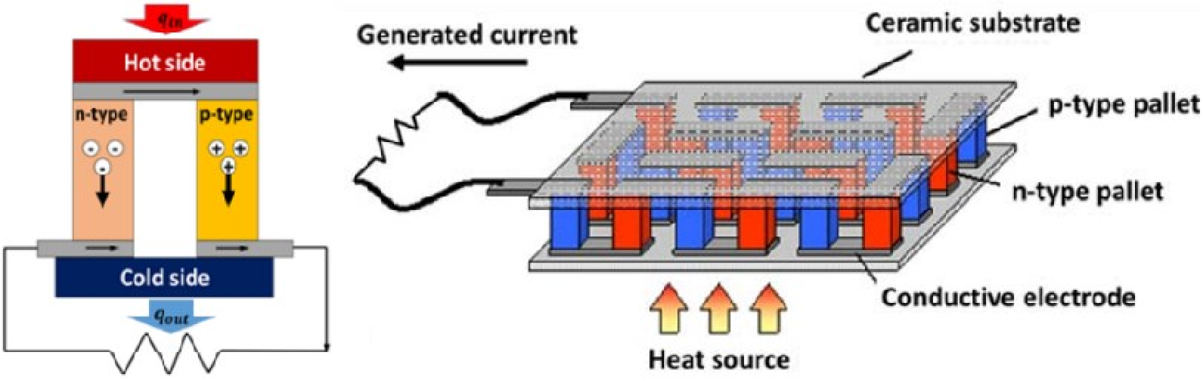

Figure 2.1: Components of a TEG module [10].

The core of a TEG is the thermoelectric material. The performance of a thermoelectric material is given by the dimensionless figure of merit ZT, defined as:

$$ZT = \frac{S_c \sigma}{k} T$$

where S_c is the Seebeck coefficient, σ is the electrical conductivity, k is the thermal conductivity, and T is the absolute temperature. This figure of merit reflects the competition between electronic and thermal transport in a material. A good thermoelectric material should have a high electrical conductivity to minimize the Joule heating effect, a high Seebeck coefficient to provide a large potential difference, and a low thermal conductivity to keep a large temperature gradient. Maximizing the figure of merit is a challenging task that involves contradictory sub-targets due to the interdependence of the factors through the carrier concentration. In particular, the electrical conductivity and the Seebeck effect exhibit an opposite dependence trend on the charge carrier concentration. Furthermore, the thermal conductivity can be deconvolved into an electronic contribution (charge carriers) and a lattice contribution (phonons), which means that increasing the electrical conductivity of a material would also lead to an increase in the thermal conductivity. Consequently, an increase in the electrical conductivity would result in an increase in thermal conductivity. Therefore, improving the ZT can only be achieved through nanostructuring approaches such as quantum confinement and decoupling of thermal and electronic transport. Unfortunately, despite continuous improvements, solid-state thermoelectrics continue to be significantly behind other heat-to-electricity technologies in terms of cost (expensive materials and difficult to synthesize) and low efficiency.

It has become necessary to work on different technologies.

2.2 Beyond Thermoelectrics

In recent decades, significant efforts have been made to research and develop alternative technologies for capturing low-grade heat. Thermal energy harvesters are solid-state devices that do not produce harmful discharge and have low maintenance cost. Despite having low energy conversion efficiency, typically 1-10%, they are self-sustaining and can be conveniently installed anywhere with minimal operational costs and space. In the following, pyroelectric energy harvesting will be examined in more detail. It is a technology that shows great potential in this field, as demonstrated by the data presented in Figure 2.2, which illustrates the number of papers published in the corresponding field from 2003-2022.

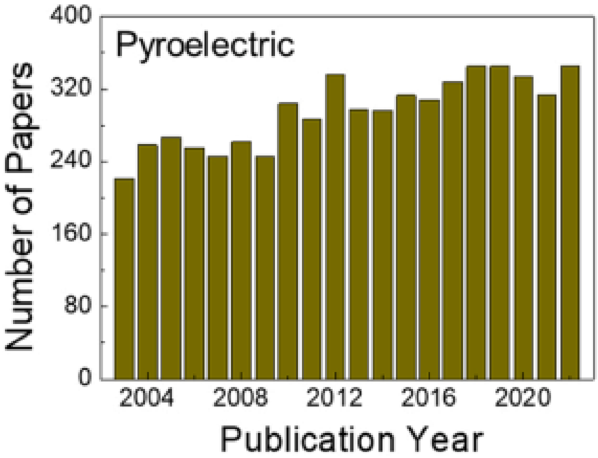

Figure 2.2: Number of papers published in the pyroelectric field from the year 2003-2022. This figure has been acquired by searching for "pyroelectric" in the titles of articles on SCOPUS.

2.2.1 Pyroelectric energy harvesting

The origin of pyroelectricity in pyroelectric materials lies in the polarization response to temperature fluctuations. Therefore, pyroelectrics can harvest energy in an environment where the temperature is spatially uniform, but time-dependent temperature variations lead to a change in the spontaneous polarization of these materials, which is used to generate current. Among the different pyroelectric materials used for thermal-energy-harvesting applications, ferroelectric-based pyroelectric materials shows superior performance. This is due to their sizeable spontaneous polarization P_s. Moreover, it is necessary that the materials used are non-centrosymmetric and polar. Figure 2.3 shows the pyroelectric material's reaction to thermal fluctuations in tetragonal (polar/ferroelectric for temperatures smaller than the Curie point T_c) and cubic (non-polar/paraelectric for temperatures larger than the Curie point T_c) structures. In the Region-I (T< Tc), a change in the temperature of the material alters the bound charges distribution. As a result, the redistribution of free charges leads to the flow of electrical current I_p within the circuit. By cycling the temperature of pyroelectric materials, current can be generated. For a pyroelectric capacitive structure the pyroelectric coefficient p of a material is defined as:

$$p = \frac{I_p}{\frac{dQ}{dt}} = \frac{I_p}{A\frac{dT}{dt}}$$

Where A is the area of the capacitor and Q is the generated pyroelectric charge. The pyroelectric coefficient (p) increases with temperature as the dipole and domain motion increase. A maximum is achieved when $T \approx T_c$ is in Region III .

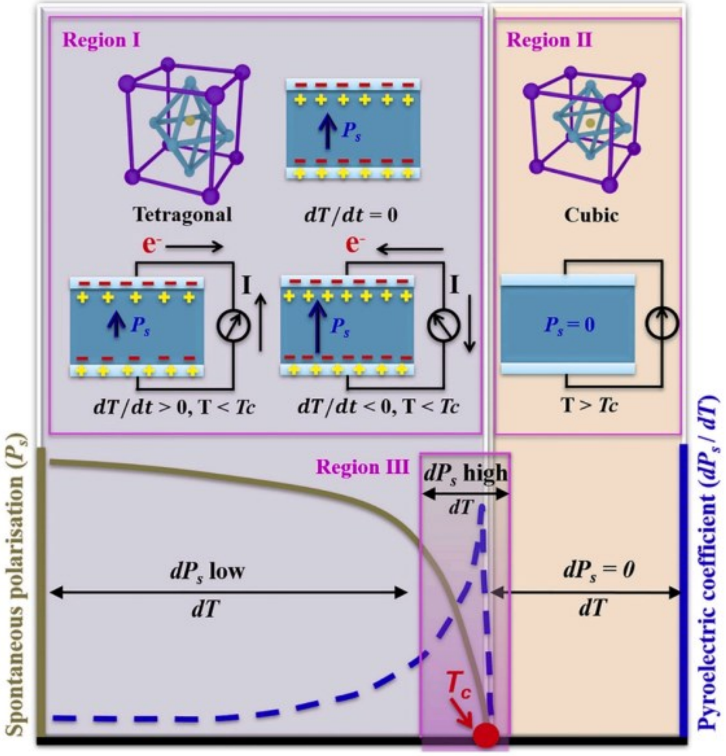

Figure 2.3: Pyroelectric material response in Region-I (T< Tc), Region-II (T> Tc), and Region-III i.e., high pyroelectric response region [8].

There are various thermodynamic cycles proposed in the literature for pyroelectric generators in order to extract potential work. One of the most common is the Ericsson cycle, illustrated in Figure 2.4.

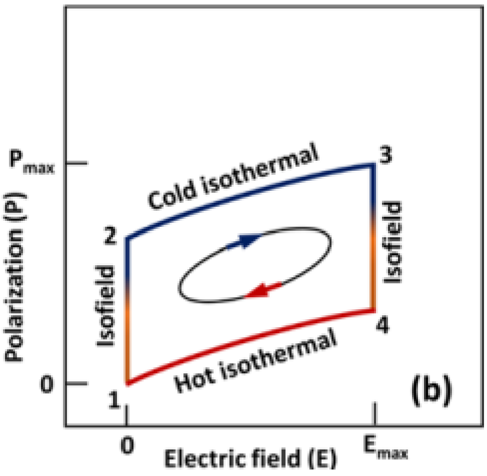

Figure 2.4: Ericsson cycle for pyroelectric generator [10].

This cycle comprises two isothermal processes, namely 2 to 3 and 4 to 1, and two constant electric field processes, namely 1 to 2 and 3 to 4. State 1 represents the pyroelectric material's initial state under zero electric field and T_h temperature. The material is cooled until it reaches temperature Tc (state 2) without any electric field. In state three, the electric field is applied and increased isothermally until it reaches the maximum value, E_{max}. This process is followed by isofield heating, in which the material is heated from state temperature T_c to T_h under a constant electric field. Finally, the electric field is reduced from E_{max} to zero while maintaining the material's temperature constant (T_h). Figure 2.5 shows, as example, a set up for Ericsson-based pyroelectric thermal-electrical energy conversion. It includes $BaTiO_3$ thin-film capacitor with electrodes. A gold strip acts as a resistive heater while located above the pyroelectric capacitor. A layer of SiO_2, positioned between the top electrode and the heater, serves as an insulator for the pyroelectric film.

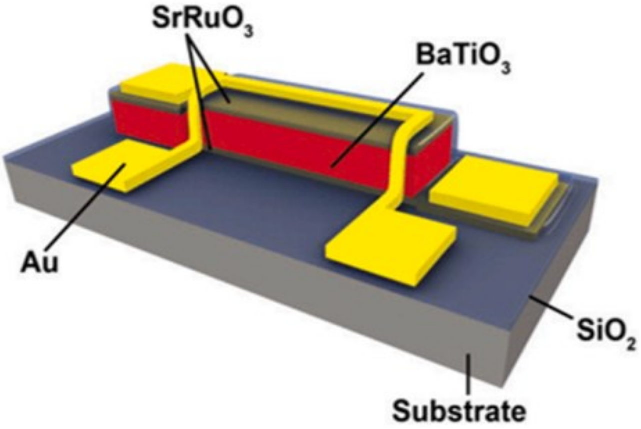

Figure 2.5: Schematics of a device consisting of a $BaTiO_3$ film to harvest the energy from pyroelectric Ericsson thermal-electrical cycles [8].

2.3 Electrochemical thermal energy harvesting

Another significant portion of the most promising technologies for low-grade thermal energy harvesting rely on electrochemistry.

2.3.1 Thermogalvanic Cells

Thermogalvanic cells, also known as thermoelectrochemical cells (TECs), represent an electrochemical equivalent of solid-state thermoelectric modules based on the Seebeck effect. The device is made up of a cell containing an electrolyte and two electrodes maintained at different temperatures, as shown in the figure 2.6.

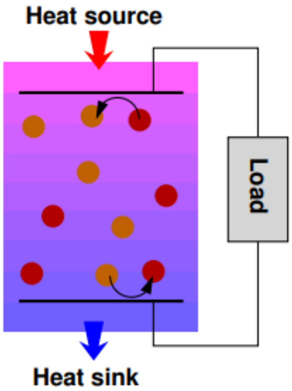

figure 2.6: Sketch of a thermogalvanic cell [11].

Essentially, a potential difference across the cell is established due to the temperature dependence of the redox potential of electrochemically active species in the cell's electrolyte medium. Temperature changes lead to a change in the entropy of the redox reaction. As a result, when a system that contains a redox-active electrolyte is exposed to a temperature difference, it generates a voltage that is proportional to the difference between the redox reactions entropies in the electrolyte near the hot and cold electrodes. Maintaining the temperature difference ensures the steady generation of voltage across the cell and the current flow when the cell is connected to an external load.

Thermogalvanic cells differ from solid-state thermoelectric devices as their mechanism involves a net transfer of material, which is absent in thermoelectric devices. In addition, a second difference is that thermogalvanic cells exploit the temperature dependence of chemical reactions that take place at electrode/electrolyte interface, rather than the kinetic energy of the electrons. It can therefore be emphasized that, inside the thermogalvanic cell, the conduction mechanism at the electrode/electrolyte interface is ionic (i.e. carried by electrolyte ions). Furthermore, the change in temperature affects not only the charge carriers, but also the solvent molecules, which influence various solute-solvent interactions, such as viscosity-induced resistance to ion motion, structure breaking of ions from their solvation shell, and solvent molecule reorientation [12].

2.3.2 Thermally regenerative electrochemical cycle systems

Thermally regenerative electrochemical cycle (TREC) systems represent a promising technology with high energy conversion efficiency for low-grade heat recovery. In this method, an electrical accumulator such as a battery or supercapacitor, is charged at one temperature and discharged at another temperature.

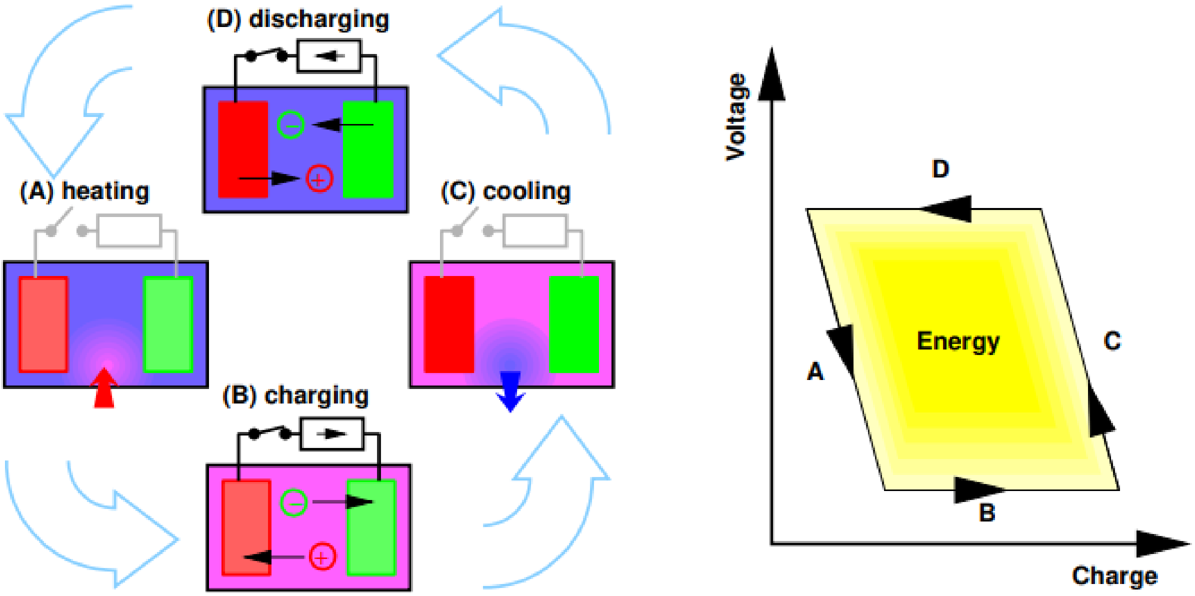

Figure 2.7: Schematic of the thermally regenerative electrochemical cycle and its representation in the voltage versus charge plot. The device is sequentially heated (A), charged (B), cooled (C) and discharged (D) [11].

The steps of this procedure, shown in Figure 2.7, are as follows:

A heating: the device is heated to T_H by the heat source;

B charging: the device is electrically charged by the external source;

C cooling: the device is cooled down to T_L by releasing heat to the heat sink;

D discharging: the device is electrically discharged through the load.

The electrode potentials change almost linearly with temperature. Two electrodes with different thermoelectric coefficients are used, so that the temperature variation of the whole cell causes the cell voltage to change. Therefore, the voltage during discharge (D) is higher than during charge (B) due to the temperature variation, while the charge flowing during the charge and discharge steps is almost the same: this results in a net energy production, which correspond to the cycle's enclosed area in figure 2.7.

Several devices have been proposed. Examples of battery-like cells with various combinations of electrodes and electrolytes include: copper versus copper hexacyanoferrate in $Cu(NO_3)_2$ solution [13]; nickel hexacyanoferrate versus Ag/AgCl in KCl solution [14]. In the case of supercapacitors, the system typically consists of active carbon based electrodes and salt solutions. The harvesting mechanism relies on the formation of the electric double layer (EDL). This methodology will be detailed in the following chapters.

Chapter 3

Supercapacitors

In this chapter, the fundamental device used in this work will be examined in detail.

Given the energy scenario outlined in Chapter 1, energy storage and harvesting technologies have been recognized as fundamental to the current society. All of these technologies can be distinguished on the basis of different parameters. The Ragone plot in figure 3.1 shows the energy and power density ranges of different storage devices.

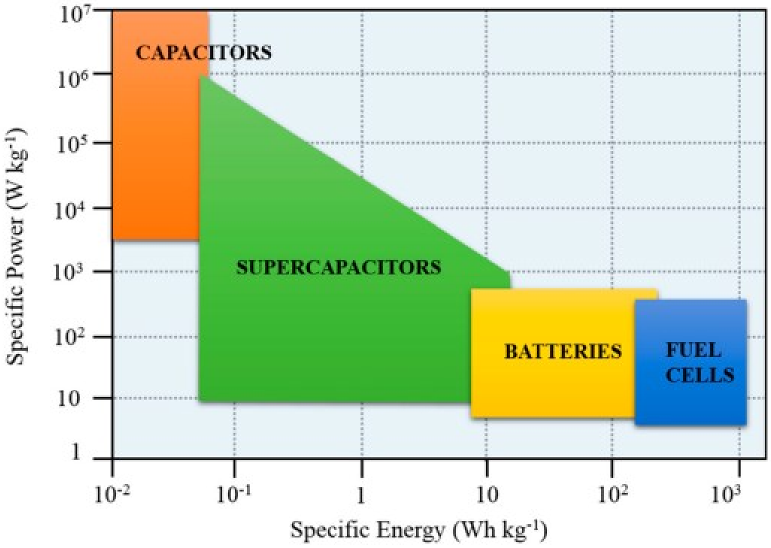

Figure 3.1: Ragone plot for different electrical energy storage devices [15].

Supercapacitors are promising candidates for energy storage applications due to their remarkable properties, including a high power density (>10 W kg^{-1}), excellent cycle lifespans (>10^6 cycles), rapid charge/discharge processes, exceptional chemical and thermal stability, and low cost. The growing interest in supercapacitors is demonstrated by the increasing number of papers published over the years, as illustrated in Figure 3.2.

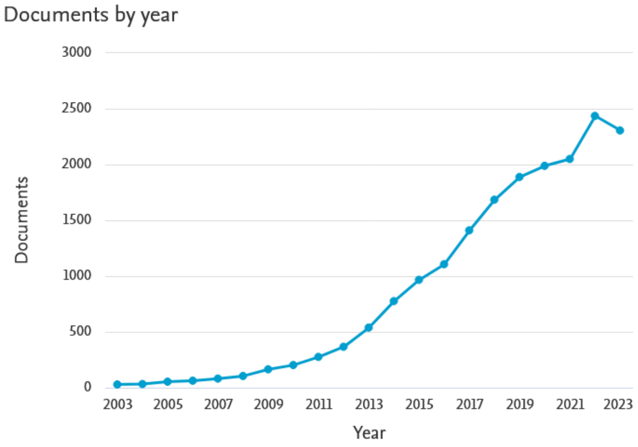

Figure 3.2: Number of papers published in the supercapacitors field from the year 2003-2023. This figure has been acquired by searching for "supercapacitor" in the titles of articles on SCOPUS.

Also known as electrochemical capacitors or ultracapacitors, supercapacitors consist of two electrodes, an ion-permeable membrane known as separator, and an electrolyte that ionically connects the two electrodes. In addition, supercapacitors have high surface area electrodes and thin dielectric separators to achieve higher capacitances than conventional capacitors. Supercapacitors can be classified into three types based on the charge storage mechanism, including electrical double layer capacitors (EDLCs), pseudocapacitors, and hybrid capacitors (Figure 3.3). More specifically, EDLCs exploit the formation of the electrical double layer (EDL) to store charge electrostatically, while pseudocapacitors store charge faradaically through redox reactions by transferring charge between electrodes and electrolytes. Lastly, hybrid supercapacitors store charge using a combination of both faradaic and non-faradaic processes.

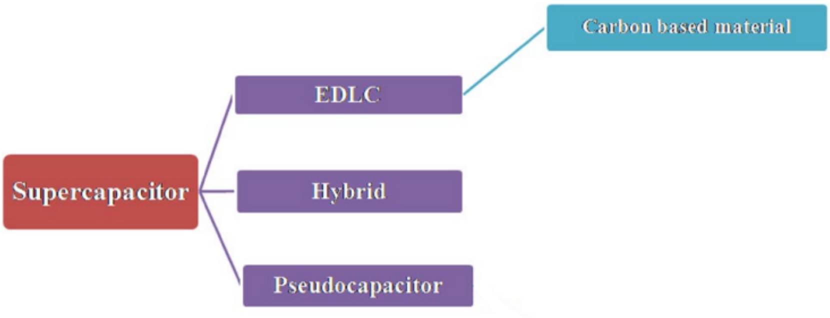

Figure 3.3: Classification of supercapacitors.

3.1 Electrical Double Layer

The working mechanism of EDLCs is founded on the concept of the Electric Double Layer, as the name suggests. The EDL is a structure that is formed when an electrolyte comes into contact with a solid surface. The double layer describes two layers of charge distributed in parallel around the solid surface. The first layer, the surface charge, typically arises from the adsorption of ions from the electrolyte or the dissociation of chemical groups on the surface. The second layer consists of ions (counter-ions) that are attracted to the surface charge through the Coulomb force, electrically screening the first layer, as shown in figure 3.4. The second layer is only loosely bound to the solid material.

The EDL was first described by Hermann von Helmholtz in 1853. He coined the term "double layer". This model depicted in Figure 3.4A is based solely on the assumption of a rigid monolayer of ions with opposite charges on the surface. Gouy and Chapman in 1913 improved Helmholz's description of the electrical double layer by incorporating the thermal movement of ions, allowing a diffuse layer of ions within the electrolyte, as shown in Fig. 3.4B. The surface charge and entropic cost of the double layer formation control the diffusion of ions. This indicates that these effects impact the thickness of the EDL. The characteristic length of the EDL is the Debye length λ_D and it depends on the on the temperature, ion charge and ion concentration. The higher the valence and concentration, the thinner the EDL becomes to balance the charge difference at the surface. This model is still inconsistent with experimental results. This is due to inaccurate assumptions, such as treating ions as point charges and assuming that ions can interact infinitely closely with the surface. Stern revised the Gouy-Chapman theory by introducing ions with a defined radius into the innermost layer of the EDL. This layer model, as depicted in Figure 3.4C, is referred to as the "Stern layer". In this model the Stern layer is defined as a compact and stagnant layer situated between the surface and the outer Helmholtz plane (OHP), which defines the average position of the charge center of solvated ions at their closest approach to the surface. On the other hand, the diffuse layer develops from the OHP towards the bulk and is composed of mobile solvated counter-ions, which in this model are still considered point charges. The boundary separating the Stern and diffuse layers is known as the slip (shear) plane, and the electric potential at this plane is referred to as the zeta potential ζ. The electric potential exponentially decreases from the shear plane towards the bulk of the electrolyte:

$$\Psi(r) = \zeta\, e^{-r/\lambda_D}$$

where r is a spatial coordinate along an axis perpendicular to the surface and $\zeta = \Psi(0)$.

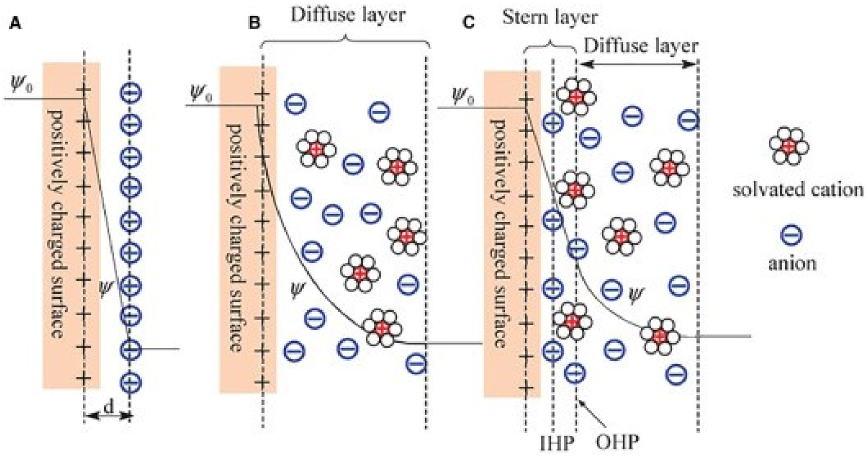

Figure 3.4: Schematic representation of the EDL using the Helmholtz (A), Gouy-Chapman (B), and Stern (C) description. IHP denotes the inner Helmholtz plane while OHP refers to the outer Helmholtz plane.

3.2 Electrical Double Layer Capacitors

EDLCs consist of two carbon-based electrodes, an electrolyte, and a separator placed between the electrodes. A schematic diagram of a typical EDLC is shown in Figure 3.5.

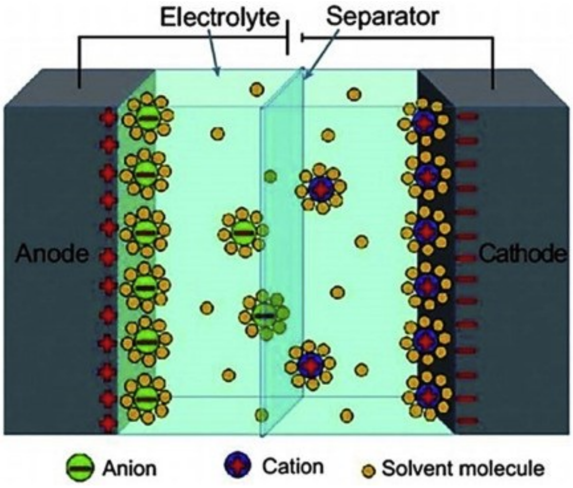

Figure 3.5: Schematic of an electrical double layer capacitor.

EDLCs store charge electrostatically and non-faradaically, meaning they do not involve any chemical oxidation-reduction reactions and do not transfer charge between the electrodes and electrolytes. EDLCs employ the electrochemical double layer of charge to store energy. As voltage is applied, charge accumulates around the electrode surfaces. Due to the natural attraction of opposite charges, solvated ions in the electrolyte solution diffuse across the separator into the pores of the oppositely charged electrodes. The EDLs at both electrodes, combined with an increase in surface area and a decrease in electrodes distance, allow EDLCs to achieve higher energy densities than conventional capacitors. The specific capacitance of EDLCs can be determined by using the following equation:

$$C = \frac{\epsilon_r \epsilon_o}{d} A$$

where ϵ_r is the relative permittivity of the EDL medium, ϵ_o is the permittivity of the vacuum, A is the specifc area of the electrode, and d is the EDL thickness. In addition, the high reversibility of charge storage mechanism in EDLCs enables them to achieve very high cycle lifespans and cycle stability. As a result, EDLCs generally operate with stable performance characteristics over many charge/discharge (CD) cycles.

Electrode materials

Electrode materials are crucial for supercapacitor performance. Carbon-based materials fully meet the supercapacitor electrode requirements. These materials, which include activated carbon, carbon nanotubes, and graphene, possess desirable chemical and physical properties such as high surface area, high porosity, low cost, and various forms such as powders, nanotubes, and aerogels. Activated carbon (AC) is the most commonly used electrode material for EDLCs. It uses a complex porous structure consisting of micropores (less than 2 nm wide), mesopores (2-50 nm), and macro-pores (greater than 50 nm) to achieve its high surface area. Experimental evidence shows that not all of the AC surface area contributes to the capacitance. This phenomenon occurs due to the size of electrolyte ions, some of which may be too large to diffuse into smaller micropores, which prevents some micropores from contributing to charge storage. Research suggests an empirical relationship between pore size distribution, energy density, and power density of the device. Larger pores are associated with higher power densities, while smaller pores are associated with higher energy densities. As a result, the pore size distribution in AC electrodes is a significant research area in the design of EDLCs [16].

Separators

Separators prevent the contact of the two electrodes. To ensure device reliability and prevent active material migration over time, a separator must be mechanically strong. Furthermore, inadequate separators can decrease the overall performance of cells by adding extra resistance. To summarize, the separators must be non-conductive and chemically resistant to corrosion from electrolytes and by-products of electrode degradation; the separator material should have good ion conductance; the electrolyte should be able to easily wet the separators. Materials such as glass, paper, and ceramics are commonly employed as separators; however, polymer-based separators are preferred due to their reasonable cost, porous nature, and flexibility [17].

3.3 EDLC electrolytes

The electrolyte is a crucial component of EDLCs due to its fundamental role in forming the EDL and consequently influencing the device's performance significantly. First of all, a major challenge for supercapacitors compared to batteries is to enhance their energy density, which depends on the capacitance C and the voltage V as follows: $E = \frac{1}{2}CV^2$. This can be accomplished by developing electrode materials with high capacitance and electrolytes with wide potential windows. In summary, the requirements for an ideal electrolyte for SCs are as follows [18]:

- Wide potential window;
- High ionic conductivity;
- High chemical and electrochemical stability;
- Wide operating temperature range;
- Environmentally friendly and low-cost.

Furthermore, the nature of the electrolyte should be considered, taking into account factors such as ion type and size, ion concentration and solvent, as well as the interactions between ions and solvent and between the electrolyte and electrode materials. As illustrated in Figure 3.6, electrolytes can be categorized mainly as liquid, solid, or quasi-solid electrolytes. Liquid electrolytes can be further classified into aqueous electrolytes, organic electrolytes, and ionic liquids (ILs). Each electrolyte has advantages and disadvantages. For instance, SCs using aqueous electrolytes exhibit high conductivity and capacitance, but their operating voltage is constrained by the narrow decomposition voltage of aqueous electrolytes. Organic electrolytes and ionic liquids (ILs) can operate at higher voltages, but typically have lower ionic conductivity. The focus will be on organic electrolytes and ILs, since they have been used in this work.

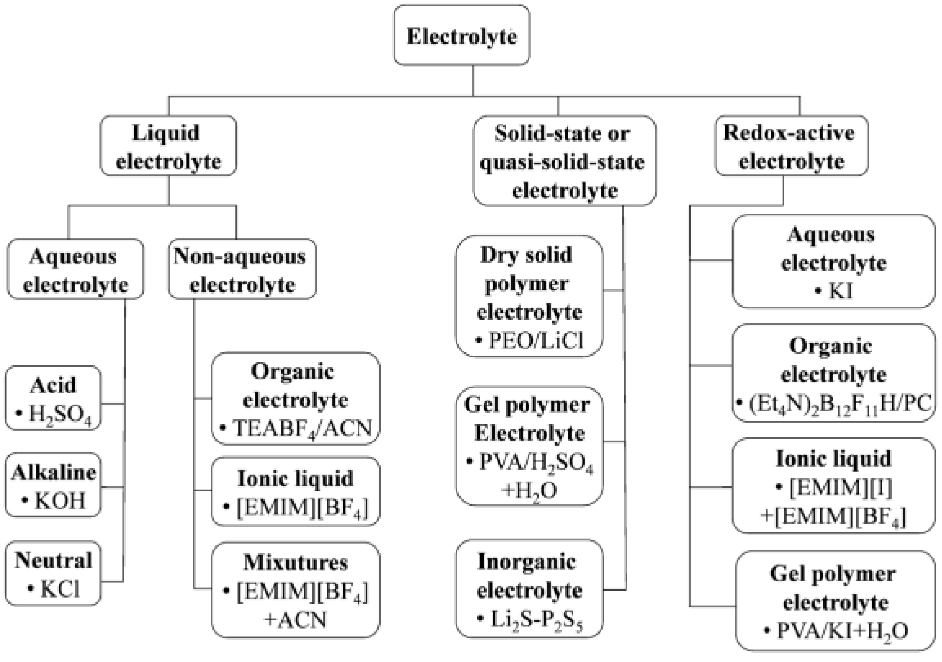

Figure 3.6: Classification of electrolytes for SCs [18].

Organic electrolytes

Organic electrolyte-based supercapacitors currently dominate the commercial market due to their high operation potential window, typically ranging from 2.5 to 2.8 V. Additionally, the use of organic electrolytes enables the utilization of less expensive materials, such as aluminum, for the current collectors and packages. Commercial EDLCs usually employ organic electrolytes comprised of conductive salts, such as tetraethylammonium tetrafluoroborate (TEABF4), that are dissolved in solvents like acetonitrile (ACN) or propylene carbonate (PC). Compared to supercapacitors (SCs) using aqueous electrolytes, SCs with organic electrolytes typically incur higher costs, smaller specific capacitance, lower conductivity, and pose safety concerns associated with their flammability, volatility, and toxicity. In addition, an organic electrolyte requires an assembly process in a controlled environment to eliminate any residual contaminants that can cause significant performance degradation [18]. The specific capacitance of an EDLC also depends on the size and distribution of pores in the carbon materials. The ability to access pores is closely linked to the properties of the organic electrolyte, including the size of the positively and negatively charged particles and their interaction with the solvent. The larger size of the majority of organic ions makes it difficult for them to access small pores, resulting in a reduction in specific capacitance. To maximize specific capacitance, it is crucial to match the size of the pores of carbon materials with the size of electrolyte ions, including solvated and bare ions [18].

Ionic liquid based electrolytes

Ionic liquids are commonly defined as salts made up exclusively of ions with melting points below 100°C. An ionic liquid typically is composed of a large asymmetric organic cation and an inorganic or organic anion. Due to their unique structures and properties, ILs have sparked significant interest as alternative electrolytes for SCs. Typically, ILs offer various advantages, including high thermal, chemical, and electrochemical stability, low volatility, and non-flammability. Furthermore, the physical and chemical properties of ILs can be significantly tailored due to the large variety of combinations of cations and anions. IL-based electrolytes compositions can be optimized or customized to meet specific requirements for SC performance, including operating cell voltage, temperature range, and ESR. This makes them an appealing choice as SCs electrolytes. ILs commonly used for SCs are based on imidazolium, pyrrolidinium, ammonium, sulfonium and phosphonium cations. Typical anions of ILs include tetrafluoroborate (BF_4^-), hexafluorophosphate (PF_6^-), bis(trifluoromethanesulfonyl)imide ($TFSI^-$) and bis(fluorosulfonyl)imide (FSI^-). Several drawbacks exist with most ILs that can limit their practical use for SCs. These drawbacks include: high viscosity and low ionic conductivity which can increase the ESR values of the IL based SC; high cost.

3.4 Supercapacitors for thermal energy harvesting

Supercapacitors constitute promising candidates for thermal energy harvesting. This thesis work is based on the concept described in the work of Hartel et al. [19], who proposed a heat-to-current converter (HTCC) based on the temperature dependence of the cell voltage of charged supercapacitors. In a similar way to thermally regenerative electrochemical cycles (TREC), the new HTCC approach exploits the temperature dependence of the electrostatic potential in a thermocapacitive charging-heating-discharging-cooling cycle to convert thermal energy into electrical energy (Fig. 3.7). Capacitive thermal energy extraction relies on increased thermal motion of ions and a related entropic change in the EDL, as shown in Figure 3.8. In this work, a commercially available SC was used in a temperature window of 0°C to 65°C. As heat reservoirs, they used a cold bath made up of an ice/water mixture maintained at a constant temperature of T_L=0°C, along with a second water bath heated to a steady temperature of T_L=0°C using a laboratory heater.

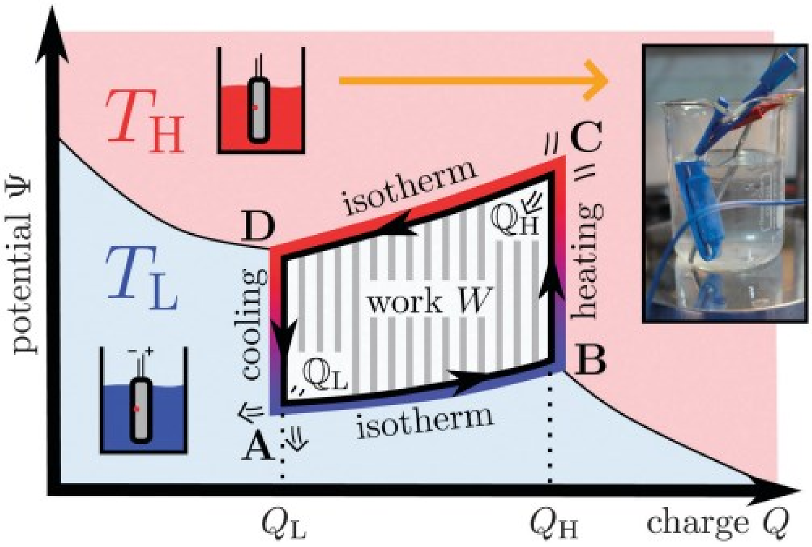

Figure 3.7: Illustration of the charging-heating-discharging-cooling cycle of the proposed HTCC [19].

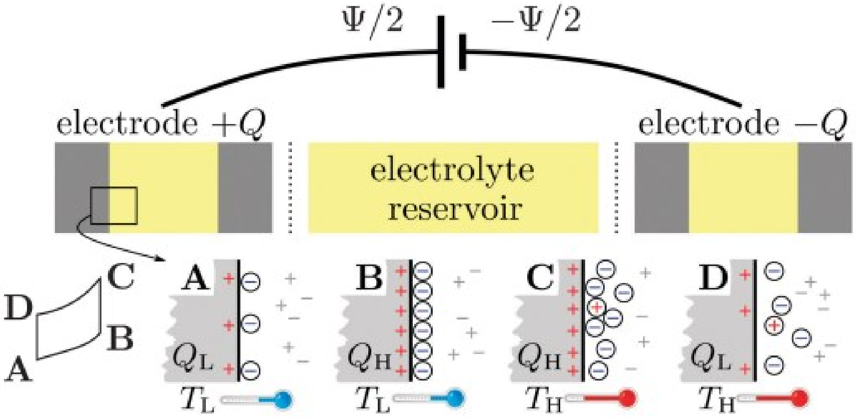

Figure 3.8: Schematic of the SC positive electrode and the EDL in each state of the ABCDA cycle at both high (H) and low (L) temperatures T and charges Q of the device [19].

Here are the steps of the procedure that was adopted:

- **A->B isothermal charging**: at T_L=0°C the device is charged in galvanostatic mode while limiting the cell voltage to 2.5 V;
- **B->C heating**: the device is placed in the heat reservoir at a temperature of T_H=65°C in open circuit mode. As a result, the thermal voltage rise (TVR) occurs instantaneously and the cell voltage reaches its maximum;

- **C->D isothermal discharging**: by keeping the cell in the hot state a cell voltage decrease is observed. This is due to the several phenomena including self-discharge and ion redistribution. The device is completely discharged to 0V at 65°C;
- **D->A cooling**: at T_L=0°C the device is cooled down.

The open-circuit potential measurements from the experiment are shown in Figure 3.9, where the TVR can be observed.

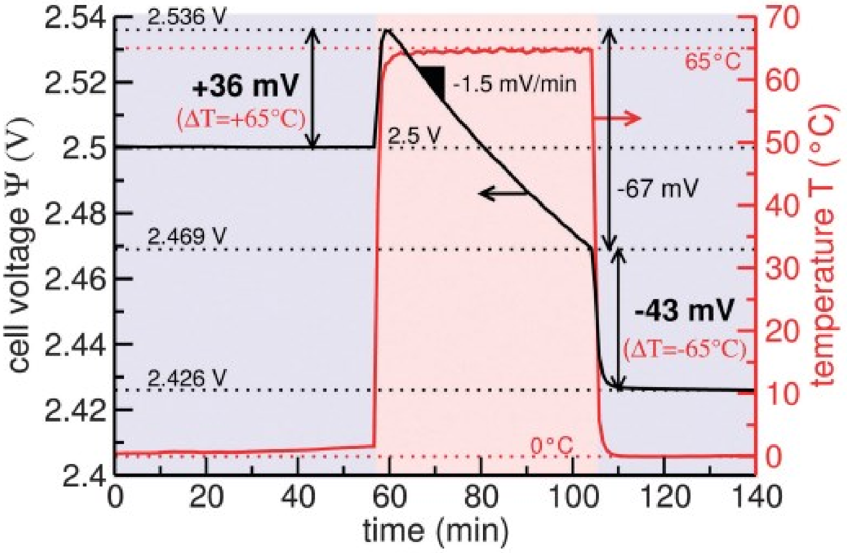

Figure 3.9: Measurement of the open circuit potential of the fully charged device when cycled between temperatures of 0°C and 65°C [19].

Essentially, the resulting cyclical change in the entropy of the system, and thus the double layer capacitance, causes a change in the open circuit potential of the charged device (the TVR), and consequently energy can be extracted from the TVR at each cycle.

Chapter 4

Materials and Methods

In the first part of this chapter, a comprehensive overview of the main figures of merit used for evaluating the performance of a supercapacitor and the employed characterization techniques is given. The second part describes the materials and equipment used for this work.

4.1 Performance evaluation parameters

The performance of a supercapacitor can be evaluated by a number of key parameters. These include cell capacitance, operating voltage, equivalent series resistance (ESR), power and energy density, coulombic and energy efficiency.

4.1.1 Specific capacitance

The total capacitance C_T of a SC is a measure of the electrical charge ΔQ stored when a voltage change ΔV is applied to the SC. It is usually preferable to use specific capacitance C_S rather than total capacitance for comparison of results in the literature:

$$C_S = \frac{\Delta Q}{\Delta V\ \Pi}$$

where Π represents the normalization factor and is typically either the mass or the surface area of the electrode material, so it can be expressed in $F\ g^{-1}\ or\ F\ cm^{-2}$, respectively. The capacitance of a SC depends on several factors such as the material and structure of the electrode, the electrolyte and the operational conditions. Of particular significance is the working voltage window.

4.1.2 Coulombic and energy efficiencies

An important parameter that indicates the stability and reproducibility of the process is the efficiency. Two distinct types of efficiencies can be distinguished: coulombic efficiency and energy efficiency. Coulombic efficiency is related to the capability of a device to deliver the majority of its stored charge. The coulombic efficiency is determined by the ratio of the charge released during the discharge to the charge stored during the charge process:

$$\eta_C = \frac{Q_{discharge}}{Q_{charge}} \bullet 100$$

Ideally, the value should be 100%, but it is not achievable because of parasitic losses. A significant source of loss is the internal series resistance of the supercapacitor, which prevents the full transfer of stored energy to the load and therefore compromises energy efficiency. The energy efficiency is defined as the ratio of the stored energy to the released one:

$$\eta_E = \frac{E_{discharge}}{E_{charge}} \bullet 100$$

These parameters and capacitance can be calculated using both CV and CCCD techniques, which will be described in the upcoming sections.

4.1.3 Equivalent series resistance

An effective approach for examining a SC is to represent it in the form of an equivalent circuit. The Randal circuit describes the SC using three distinct elements: resistor (R), capacitance (C), and inductor (L). Typically, the inductor can be neglected because it only describes the pseudo-inductance of the connecting wires, which is only relevant at high frequencies. In figure 4.1 it is shown the schematics of a first simplified model [20].

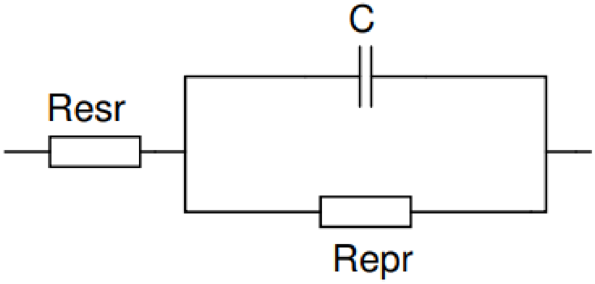

Figure 4.1: Simplified Randles circuit [21].

Where C represents the total capacitance, R_{ESR} considers electrode and ionic electrolyte resistance, and R_{EPR} is the equivalent parallel resistance that takes into account system leakages. The R_{ESR} is affected by several device parameters such as electrolyte conductivity, contact resistances, or electrode/electrolyte interfaces. Generally, it is preferable for the ESR value to be as small as possible. Generally, the ESR value is typically obtained through the use of EIS technique, which will be discussed in the following section.

4.2 Characterization methods

This section discusses the methods used to characterize the electrolyte and the device. Firstly, an overview of electrolyte characterization methods is given to determine some chemical-physical properties of the electrolytes such as conductivity and viscosity. In the second part of the chapter, the electrochemical characterization techniques used to characterize the supercapacitors are analyzed. Finally, the instruments used and the fabrication processes of the devices used are described.

4.2.1 Conductivity measurement

To determine the electrolyte conductivity σ, a conductivity cell was used. Figure 4.2 depicts the 192/K1 conductivity cell, designed by AMEL Electrochemistry, which consists of a glass body containing the solution to be analyzed and two parallel plates platinum-based electrodes separated by a fixed distance.

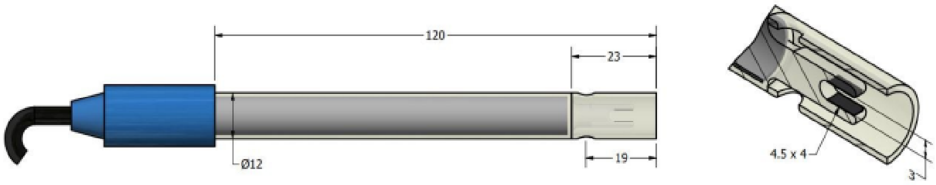

Figure 4.2: Conductivity cell 192/K1 structure [22].

The potentiostat is connected to the cell and impedance spectroscopy (EIS) is performed to determine the electrolyte resistivity by evaluating the ESR. The electrolyte conductance G is defined as:

$$G = \frac{1}{ESR}$$

Eventually, the electrolyte conductivity σ is determined as:

$$\sigma = \frac{G}{K}$$

where K is a constant determined by the conductivity cell’s geometry, specifically as the ratio between the surface of the electrodes and the distance between them.

4.2.2 Viscosity measurement

To measure the viscosity of the electrolyte, a rheometer was used. Figure 4.3 illustrates the specific rheometer employed, the MCR 302 by Anton Paar. The operating principles of this instrument are as follows: the material under investigation is placed between two parallel plates in the rheometer. The rheometer systematically varies the shear rate applied to the material. As the shear rate is varied, the rheometer measures the corresponding stress response of the material. Stress is the force applied per unit area, and it provides information about the material's resistance to deformation. The relationship between shear rate and stress is used to calculate the viscosity of the material at different points in the shear rate ramp. This device allows to vary several parameters in order to study the material under different conditions, in particular during these measurements the temperature and the shear rate were varied.

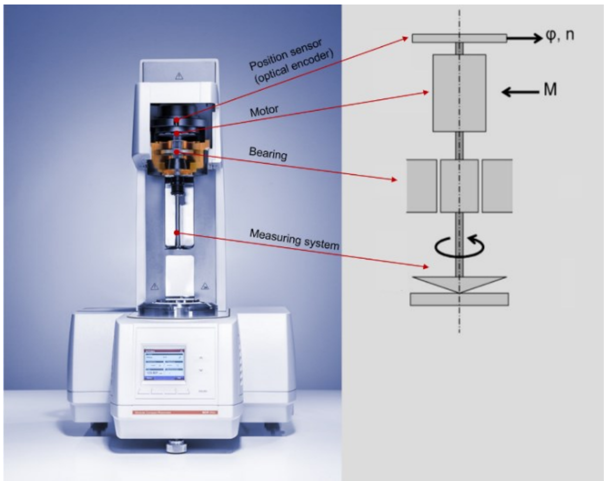

Figure 4.3: Anton Paar's MCR 302 [23].

4.2.3 Electrochemical characterization methods

Cyclic Voltammetry (CV)

Cyclic Voltammetry (CV) is an electrochemical technique widely used to characterize the performance of supercapacitors. It can be carried out with a two-electrode configuration or with a three-electrode configuration, depending on the type of evaluation of interest. The potential across the electrodes is swept linearly with a specified periodicity defined by the chosen scan rate. The input voltage is illustrated in Figure 4.3a. The characteristic plot of a CV experiment is a cyclic voltammogram (figure 4.3 c), which is a graph showing the relationship between the applied potential and the resulting current.

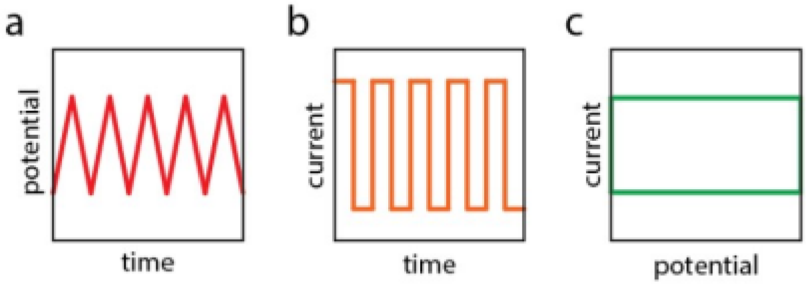

Figure 4.3: Cyclic voltammetry signals [24].

For EDLCs the ideal shape of a voltammogram is rectangular. Non-idealities, such as parasitic effects and material degradation, impact the behavior of the EDLC, some of which are reflected in the voltammogram. For instance, the system's resistivity induces a corner rounding of the CV, which results in a leaf-like shape. Additionally, degradation of the electrolyte is also visible in the CV plot. Specifically, this degradation results in horn-shaped features in the higher voltage regions of the voltammogram. Furthermore, coulombic efficiency, energy efficiency and specific capacitance can be determined by integrating CV curves. The capacitance can be calculated as follows:

$$C = \frac{1}{\nu 2\Delta V}\int_{V_{min}}^{V_{max}} i(\nu)d\nu$$

where ν is the scan rate.

Electrochemical Impedance Spectroscopy (EIS)

This technique is used for performing an analysis of impedance spectrum. In general, the system is perturbed by an input voltage that is a superposition of a small amplitude sinusoidal (time dependent) voltage $v_s(\omega)$ and a DC voltage V_{DC}:

$$V_{applied} = V_{DC} + v_s(\omega)$$

The output current is time dependent as well and the resulting impedance can be written as:

$$Z(\omega) = Z'(\omega) + jZ''(\omega)$$

Where $Z(\omega)$ is a complex function of the frequency ω and it can be represented in a complex plane with the real part on the x-axis and the imaginary part on the y-axis. This type of representation is referred to as the Nyquist representation or Nyquist plot.

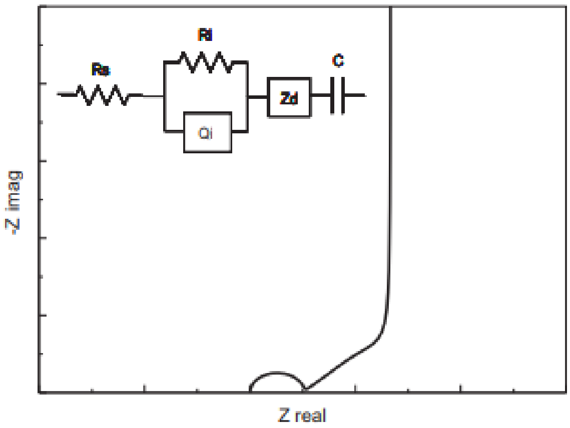

Figure 4.4: Typical Nyquist plot for a carbon based electrode EDLC and equivalent circuit [25].

Figure 4.4 shows the typical Nyquist plot for a carbon based electrode EDLC and the equivalent circuit. Two figures of merit may be used to describe the EDLC resistivity behavior: the equivalent distributed resistance (EDR) and the ESR. The ESR refers to the resistivity associated with the electrodes, bulk electrolyte, and contacts, whereas the EDR refers to the difficulty for the electrolyte to diffuse inside the pores. It is possible to identify the resistive and capacitive behavior of the SC using the equivalent circuit shown in figure 4.4: the series resistance term (ESR) determines the impedance at high frequencies, whereas the capacitance is negligible. The resistive term is negligible in the low frequency region and the capacitive behavior predominates (vertical line). The semicircle in the Nyquist plot can be associated to the poor contact between the current collector and the composite electrode. The semicircle observed in the Nyquist plot can be associated to the poor contact between the composite electrode and the current collector [25].

Constant current charge/discharge (CCCD)

A CCCD test consists in a charging/discharging loop between two defined voltages by applying a constant current to the device. The potential resulting from this is plotted as a function of time. Ideally, the response has a triangular shape (figure 4.5A) and the two opposite slopes define the charge and the discharge processes.

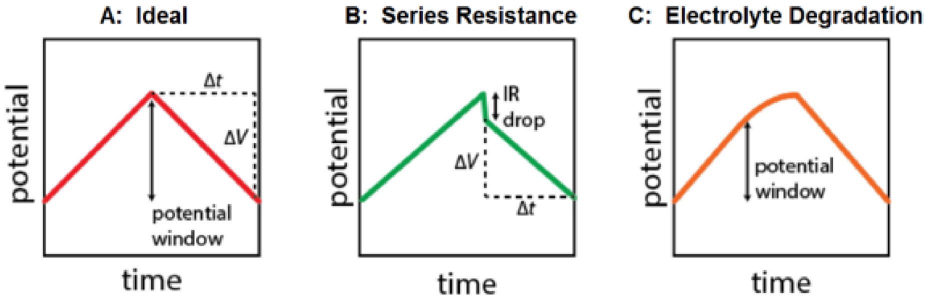

Figure 4.5: Galvanostatic charge/discharge plots [24].

The capacitance of the supercapacitor can be calculated as:

$$C = \frac{I}{\Delta V / \Delta t}$$

Where I is the applied current magnitude and $\Delta V / \Delta t$ is the discharge curve's slope. Non-idealities result in a non-linear response, which modifies the capacitance as well. For instance, when the device switches from the charge to the discharge state, an high series resistance (ESR) can cause a voltage drop (IR drop) (fig. 4.5B). Furthermore, electrolyte degradation causes inflection points in the trend and a blurred transition between charge and discharge (fig. 4.5C).

4.3 Fabrication steps and experimental setup

This section provides a description of the fabrication process for supercapacitors, including the materials and equipment used.

Electrodes

First, a slurry is prepared starting from the following materials:

- Activated carbons (AC): the active component where the energy storage occurs. They have a high surface area (up to 3000 m^2g^{-1}), low conductivity and high density;
- Carbon black (CB): it has high conductivity, low high to surface area and low density.
- Binder: it enables the adhesion to the current collector and cohesion between particles. A binary binder consisting of carboxymethyl cellulose (CMC) and styrene-butadiene rubber (SBR) was used for this purpose.

The weight percentage of these materials in the overall slurry is as follows: 85% AC, 10% CB, 2.5% CMC and 2.5% SBR. Distilled water was used initially to dissolve the binder. The mixture was then stirred at 800rpm and heated up to about 60°C to favor solvent evaporation. The remaining components were added gradually, and the mixture was subsequently mixed once more at 800rpm for approximately 24 hours until a homogeneous mixture was achieved. In order to prepare the complete electrode, a current collector is required. In this case, aluminum was used as the current collector material. The slurry prepared was then manually coated with a doctor blade (fig. 4.6). Following this, the coated slurry was left to dry overnight at room temperature. Next, the electrode is cut into 15mm diameter disks using a puncher. The final step is to dry the disks for 6 hours at 120°C in a BUCHI glass oven B-585.

Figure 4.6: Photograph of an electrode after doctor blade coating of carbon slurry.

Electrolytes

Three electrolytes were used: the organic salts tetraethylammonium tetrafluroroborate (Et_4NBF_4 or $TEABF_4$) and tetraethylammonium bis(trifluoromethane)sulfonylimide (Et_4NTFSI or TEATFSI) and the ionic liquid N-methyl-N-butylpyrrolidinium bis(trifluoromethane)sulfonylimide ([Pyr_{14}][TFSI]). As a solvent, propylene carbonate (PC) was chosen. Different concentrations were considered for all the electrolytes. They were prepared in a safe environment in order to operate within an inert atmosphere. A LABstar pro glovebox by MBRAUN was used for this purpose. The glovebox atmosphere contains less than 1 part per million of both moisture and oxygen, thanks to the gas purification system. The equipment also includes a vacuum pump and two ante-chambers, which allows for the safe introduction of multiple objects without contamination of the atmosphere.

Separators

Separators are porous materials that are used to prevent direct electrical contact between the electrodes while allowing rapid transport of electrolyte ions. They play a crucial role in determining the overall performance of the supercapacitor. Separators must meet a number of requirements: they must be thin, chemically stable, porous and mechanically robust. Glass fiber separators were used for this purpose, specifically Whatman Grade GF/D, which have a thickness of $675\,\mu$. Finally, the separators were cut into 15mm diameter disks using a puncher.

Coin cell

The packaging must meet several requirements: ensure proper mechanical stress, minimize resistance, provide electrical isolation, ensure agency compliance, and increase overall cell reliability. Finally, a coin cell was assembled. The components of a coin cell are shown in figure 4.7:

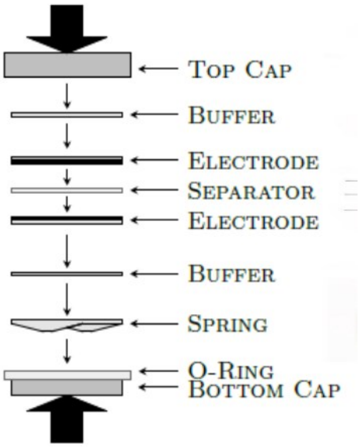

Figure 4.7: Schematic of a coin cell.

The cell was assembled in the glovebox. Electrodes with the same mass were chosen in order to ensure a symmetric device. For each coin cell, the separator was wetted with an amount of $200\,\mu l$ of electrolyte. Once assembled, the cell was removed from the glovebox and sealed with a crimper.

Pouch cell

Another setup was tested. Pouch cells were assembled. For this purpose, the electrodes were cut to form a rectangular shape of 2cm x 6cm, which resulted in an active are of 12cm^2. Each electrode was attached to an aluminum strip to serve as an electrical terminal. The separator was also cut to create a rectangular shape measuring 2.5cm x 6.5cm. It was positioned between the two electrodes, which were aligned to increase the overlapping area of active material. The entire assembly was then placed in a pouch bag. Subsequently, approximately $1.4ml$ of electrolyte was used to wet the separator, and finally the pouch cell was vacuum sealed. As with the coin cell process, the pouch cell was assembled and sealed inside the glovebox. In Figure 4.8, a photograph of some of the fabricated pouch cells is shown.

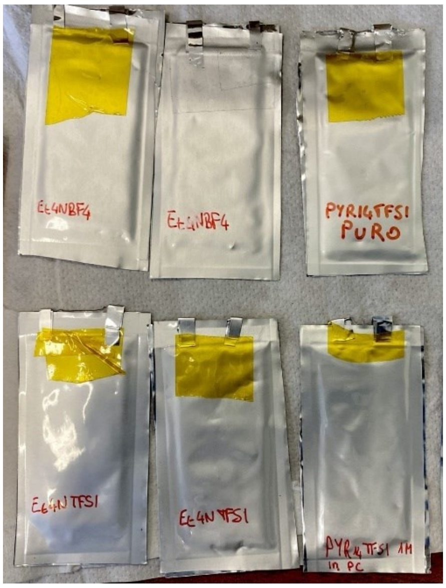

Figure 4.8: Photograph of some of the manufactured pouch cells.

Chapter 5

Results

This thesis is built on the idea described in the work of Hartel et al. [19], where a commercially available SC was used for a new type of HTCC. In this study some assumptions were made in order to maximize the efficiency of the method employed, for example, it proposed a guideline for the selection of materials to be used: low heat capacity, high pseudo-Seebeck sensitivity and large charge capacity [19]. However, a more in-depth investigation was not carried out. The purpose of this thesis is to try to find ways to make this type of harvesting process more efficient through the engineering of the device. The aim is to study some physico-chemical properties of the selected electrolytes at different temperatures. Among these, in particular, are the viscosity and the conductivity. Furthermore, the role and impact of ionic association is investigated. Finally, the possible influences and correlations of these properties on the device's operation were examined. A series of electrolyte characterizations, followed by electrochemical characterizations of EDLCs, were performed. Eventually, the device is used to perform a thermocapacitive cycle of charging, heating, discharging, and cooling within a temperature range of 0°C to 80°C to harvest thermal energy.

5.1 Electrolytes characterization

Three electrolytes have been investigated in this work: tetraethylammonium tetrafluroroborate (Et_4NBF_4 or $TEABF_4$), tetraethylammonium bis(trifluoromethane)sulfonylimide (Et_4NTFSI or TEATFSI) and N-methyl-N-butylpyrrolidinium bis(trifluoromethane)sulfonylimide ($[Pyr_{14}][TFSI]$) in PC. The behavior of these electrolytes has been studied in a temperature range from 10°C to 80°C, with a step of 10°C. In addition, different concentrations of salts and ionic liquids have been considered.

5.1.1 Ionic conductivity

A conductivity cell is used to measure the conductivity of an electrolyte. The resistivity of the electrolyte can be determined through an impedance spectroscopy (EIS) by evaluating the ESR. The conductance G is given as:

$$G = \frac{1}{R}$$

Eventually the electrolyte conductivity σ is determined as:

$$\sigma = \frac{G}{K}$$

where K is a constant that depends on the geometry of the conductivity cell used for the measurement. The frequency range examined spans from 10 mHz to 1 MHz, with 10 data points per decade. As a first step the conductivities of $TEABF_4$ and $[PYR_{14}][TFSI]$ at different concentrations in PC were measured. The molarity values of the $TEABF_4$ in the solution considered were: 0.1, 0.158, 0.251, 0.398, 0.631, 1. The molarity values of the $[PYR_{14}][TFSI]$ in the solution considered were: 0.1, 0.158, 0.251, 0.398, 0.631, 1, 1.585, 2.512. These specific concentration values were chosen in order to obtain a logarithmic fit. In the latter case also the pure ionic liquid was also characterized. In the first case, however, the increase in salt concentration is limited by the solubility limit. Figure 5.1 shows the conductivity of electrolytes as a function of molarity. These measurements were performed at 25°C. In the TEATFSI case, the measurements are not reliable due to problems during the measurements, they should be repeated.

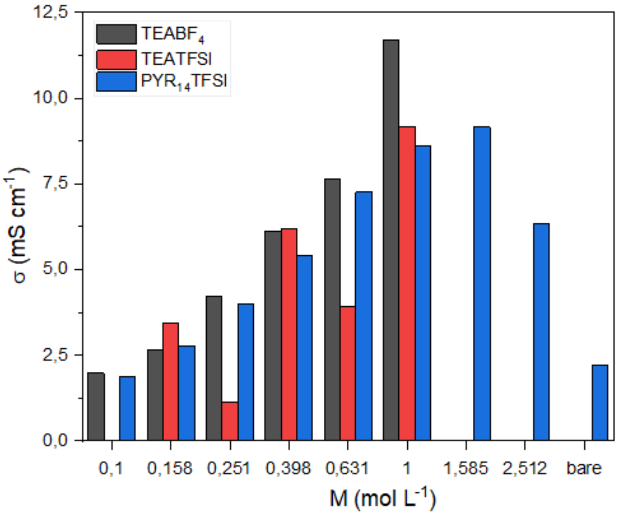

Figure 5.1: Conductivities of TEABF$_4$, TEATFSI and [PYR$_{14}$][TFSI] in PC as a function of molarity.

The system's conductivity increases as the electrolyte concentration increases at a constant temperature. It reaches a certain level and then tends to decrease. The main reason is that as the electrolyte concentration increases, on the one hand, the distance between anions and cations in the solution decreases, and on the other hand, some anions and cations form non-conducting ion pairs, which leads to a decrease in the number of free ions participating in conduction.

The conductivity's temperature dependence was subsequently examined. The temperature range under evaluation spans from 10°C to 80°C with a 10°C degree increment. In a first case the same conductivity measurements were performed by considering 1M solutions of TEABF$_4$, TEATFSI and [PYR$_{14}$][TFSI] in PC (fig. 5.2), since conductivities were overall higher in 1M solutions, as shown in figure 5.1. The TEABF$_4$ solution exhibits higher overall conductivity values. This behavior may be attributed to the ions' size involved in the diffusion process. Table 5.1 displays the size of the analyzed ions in increasing order from the smallest to the largest: $BF_4^- < TEA^+ < TFSI^- < Pyr_{14}^+$. It follows that TEABF$_4$ is the salt containing the smallest ions, which makes them more contributing to the ionic conductivity [26].

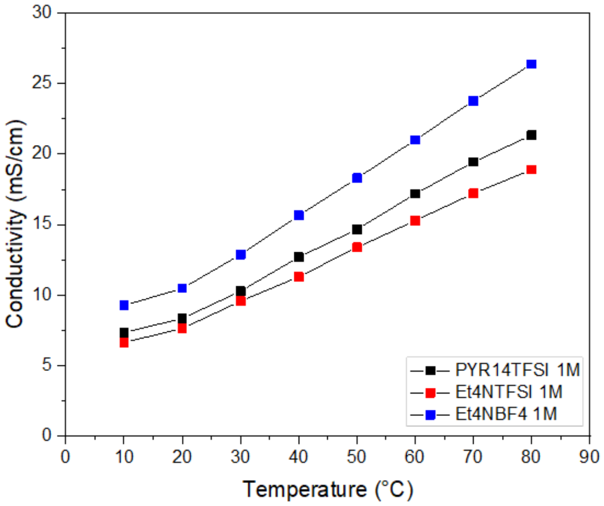

Figure 5.2: Conductivity as a function of the temperature for different electrolytes.

Table 5.1: electrolytes properties at 20°C [22].

Electrolyte	Ion size (nm)	
	Cation	Anion
1M $TEABF_4$ in PC	0.69	0.46
1M TEATFSI in PC	0.69	0.7
1M $PYR_{14}TFSI$ in PC	1.1	0.7

Electrical conductivity is a transport property of ions and it depends sensitively on temperature. The conductivity of a solution basically increases with temperature because the mobility of the ions increases. The conductivity of a thermally activated ion-transport process can be described by a simple Arrhenius expression:

$$\sigma = \sigma_0 e^{-E_a/RT}$$

Where the exponential prefactor σ_0 is constant, the quantity E_a is the activation energy for the thermally activated process, R is the universal gas constant and T is the absolute temperature.

Further conductivity measurements were then made using solutions of different concentrations of $[PYR_{14}][TFSI]$ in PC at different temperatures i.e., from 10°C to 80°C (fig. 5.3).

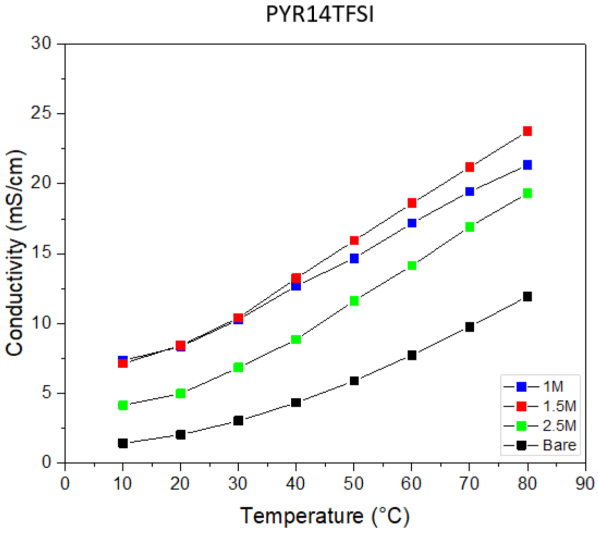

Figure 5.3: Conductivity as a function of the temperature for solutions of different concentrations of $[PYR_{14}][TFSI]$ in PC.

5.1.2 Viscosity

Afterwards, the viscosity was evaluated as a function of temperature. The temperature range under evaluation spans from 20°C to 80°C with a 20°C degree increment. The measure was set as follows: for each temperature, 20 measurement points were obtained by applying a logarithmic shear rate ramp ranging from 10 to 1000 rad/s. As can be seen in figure 5.4, this temperature dependence typically sharply rises at low temperatures but gradually becomes smoother as the temperature rises.

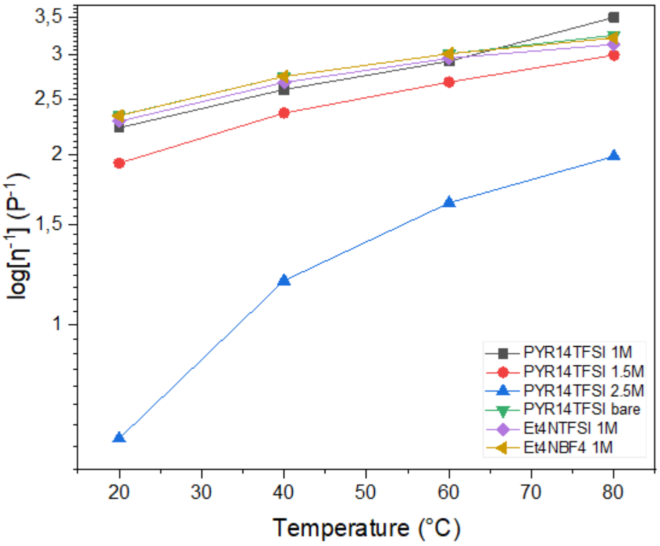

Figure 5.4: Viscosity as a function of the temperature for solutions of different concentrations of $[PYR_{14}][TFSI]$ and for 1M $TEABF_4$, TEATFSI in PC .

The viscosity's temperature dependence can be determined approximately from rate theory by introducing a potential energy barrier which must be overcome by liquid molecules in order to jump and occupy the free volume sites as they move through the liquid [27]. Thus, an

Arrhenius like equation is typically used to represent the viscosity of liquids as a function of temperature:

$$\eta = \eta_0 e^{-E_a/RT}$$

where η_0 is a constant and E_a is the activation energy. However, it is known that the temperature dependence of IL viscosity shows deviation from Arrhenius behavior [2]. The Vogel-Fulcher-Tammann (VFT) equation frequently finds use in describing highly viscous and glass-forming liquids, including ILs [27,28]:

$$\eta = Ae^{B/T-T_0}$$

where A is a pre-exponential factor and B and To are specific substance dependent parameters.

5.1.3 Walden plot

The conductivity and viscosity data can be further analyzed by means of the fractional Walden rule and the Walden plot. Walden rule states that for extremely diluted electrolyte solutions, the product of the limiting molar conductivity Λ_m^0 and the viscosity of the pure solvent η is constant:

$$\Lambda_m^0\, \eta = C = constant$$

$$\log \Lambda_m^0 = \log(C) + \log \eta^{-1}$$

It has been experimentally proven that the Walden rule still holds for solutions of large and weakly coordinating ions in solvents with non-specific ion-solvent interactions [24]. In this case, ion mobility and thus conductivity are exclusively determined by ion migration, as follows from the Stokes-Einstein equation [28]:

$$D_i = u_i\, k\, T$$

Where D_i is the diffusion coefficient of an ion i, u_i is its mobility, k is the Boltzmann's constant and T is the absolute temperature. It is worth noting that the single-ion mobility is related to the single-ion conductivity.

Numerous studies have provided evidence that indicates the applicability of Walden's rule to concentrated electrolyte solutions [3]. According to the Walden rule, the relation between solvents' viscosities and electrolytes' limiting molar conductivities can be represented in a logarithmic plot, called the Walden plot. The Walden plot can be used to show the conductivity-viscosity relationship of pure ionic liquids (ILs) and to infer the extent of ion association by comparing the IL's plot with that of a so-called ideal electrolyte solution, commonly a 0.01M aqueous KCl solution, in which the ions are fully dissociated and have equal mobility. Furthermore, if a group of points on the graph for the same liquid are close to the reference line, they represent "good ionic" liquids (higher ionic dissociation), while those far from the diagonal in the lower part represent "poor ionic" liquids (lower ionic dissociation) [29,30].

Deviations from the Walden rule are treated in terms of the ionicity of the ILs. The decrease in ionicity (i.e. by association) leads to an increasing deviation from the Walden rule.

According to the Walden plot depicted in Figure 5.5, it is possible to conclude that all the electrolytes below the ideal KCl line have low ionicity. Only the $[PYR_{14}][TFSI]$ 2.5M in PC is superionic.

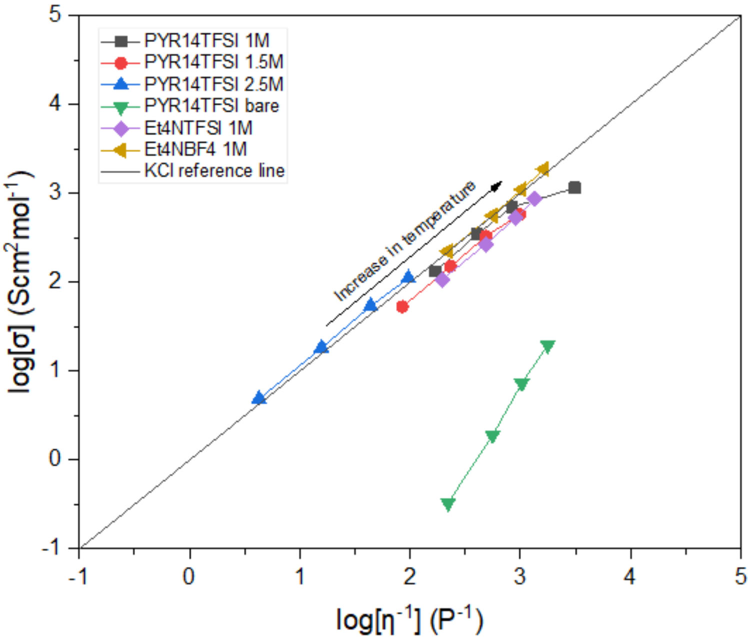

Figure 5.5: Walden plot for solutions with different concentrations of $[PYR_{14}][TFSI]$ and for 1M $TEABF_4$, TEATFSI in PC. The temperature range goes from 20°C to 80°C in 20°C increments.

Furthermore, by considering the conductivity and viscosity as Arrhenius processes, it can be stated that a positive correlation exists between the activation energy and curve slope on the Walden plot. This is due to their exponential dependency on activation energy. Therefore, a similar slope for the dissolved electrolytes implies that all of them have a similar activation energy for ionic transport. Notably, the activation energy for the bare ionic liquid $[PYR_{14}][TFSI]$ is higher than for the other dilute cases, as expected, since ion association is more favored.

In the following sections, these results are evaluated in correlation with the results obtained from the device operating condition.

5.2 Electrochemical EDLCs characterization

First, supercapacitors were assembled in a coin cell configuration and characterized by electrochemical characterization techniques. Supercapacitors containing different electrolytes were analyzed. The electrolytes used are: $TEABF_4$ 1M in PC, TEATFSI 1M in PC, $[PYR_{14}][TFSI]$ 1, 1.585, 2.512 M in PC and bare $[PYR_{14}][TFSI]$. A CCCD test (constant current charge/discharge) was performed. The procedure adopted includes the following steps:

1. OCV for 1 hour and 30 minutes;
2. Charge: a constant current of 3mA charges the SC in each voltage range until the maximum voltage is reached. The voltage ranges are between 0 V and V_{max}, where V_{max} equals a value of either 0.5, 1, 1.5, 2, or 2.5 V;

3. Discharge: a constant current of -3mA discharges the SC in each voltage range until the voltage reaches the value 0.

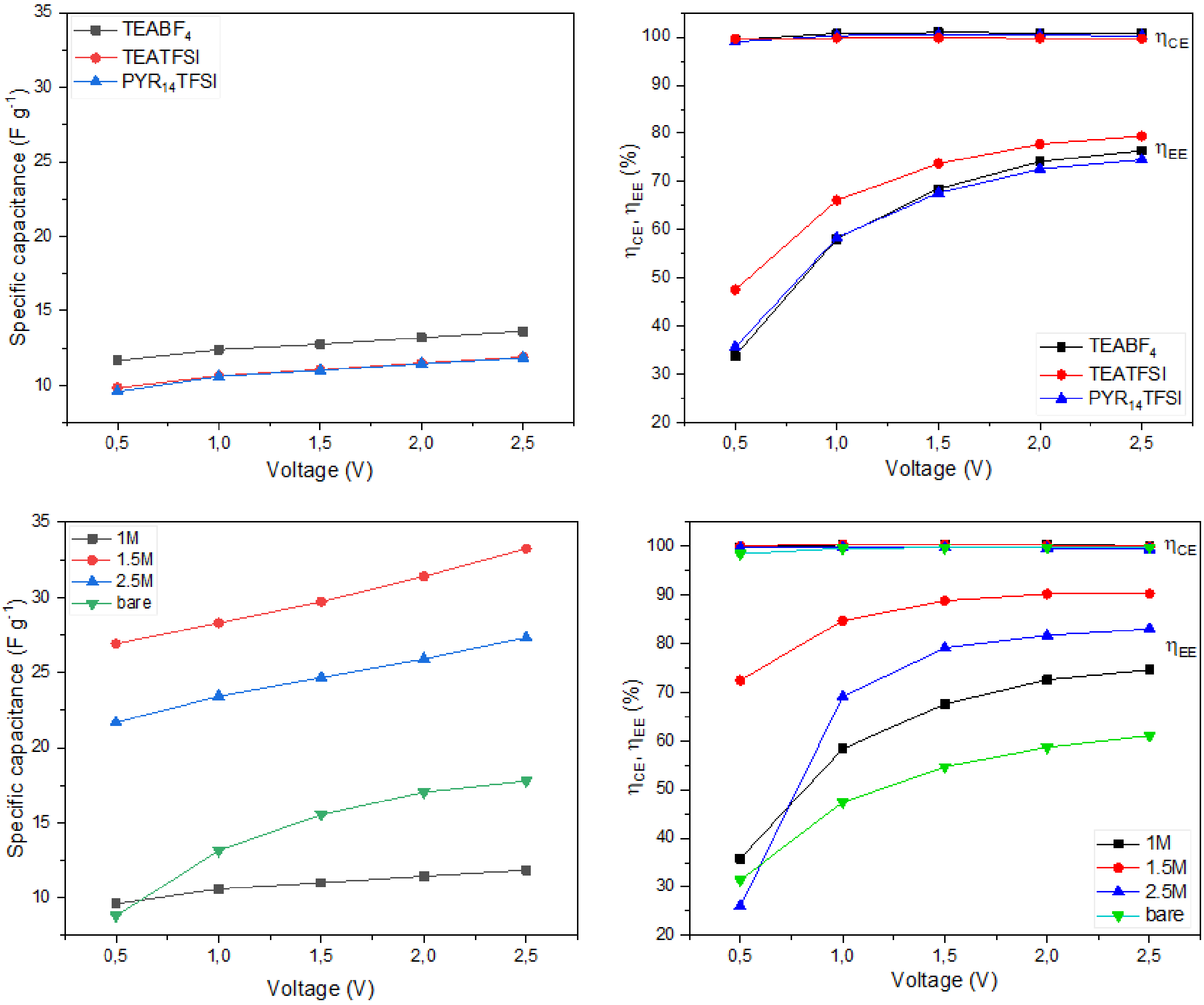

Figure 5.6: Specific capacitance, coulombic and energy efficiencies voltage dependency for SCs containing $TEABF_4$ 1M in PC, TEATFSI 1M in PC, $[PYR_{14}][TFSI]$ 1, 1.585, 2.512 M in PC and bare $[PYR_{14}][TFSI]$.

For each voltage range 50 cycles (steps 2 and 3) of charge and discharge were performed. The data obtained was used to calculate specific capacitance, coulombic efficiency, and energy efficiency. These parameters are presented in Figure 5.6, which illustrates their voltage dependence. Overall coulombic efficiencies are high, above 99% for all cells.

5.2.1 Leakage current and self-discharge

After the CCCD test, a procedure was implemented in order to evaluate the leakage current and the self-discharge.

The leakage current $I_{leakage}$ is another important parameter to consider and is related to the amount of charge lost during the operating state of the device. It is a problem since it contributes to unwanted faster discharge of the SC. To evaluate the leakage current the following procedure was adopted: the SC was charged with a constant current of about 3mA until a V_{max} was reached (V_{max} is a value of either 0.5, 1, 1.5, 2, or 2.5 V), the voltage was kept constant during a 10 minutes float time, then the value of the current was recorded and the I_{leakag} was evaluated as the last value of the current after the float time.

In the next step the SC was kept in an open circuit condition in order to evaluate the decreasing open circuit voltage which is related to the self discharge phenomenon. The self discharge results from leakage currents and charge redistribution, which in turn is reflected in the cell voltage variation over time and is affected by the initial voltage of the device and the temperature. Also in this case 5 initial voltages V_{max} were considered.

The dependence of the leakage current on voltage is emphasized in figure 5.7. The higher the SC voltage during the float time, the greater the resulting leakage current. Additionally, a faster decrease of current during the float time is observed for lower float voltages.

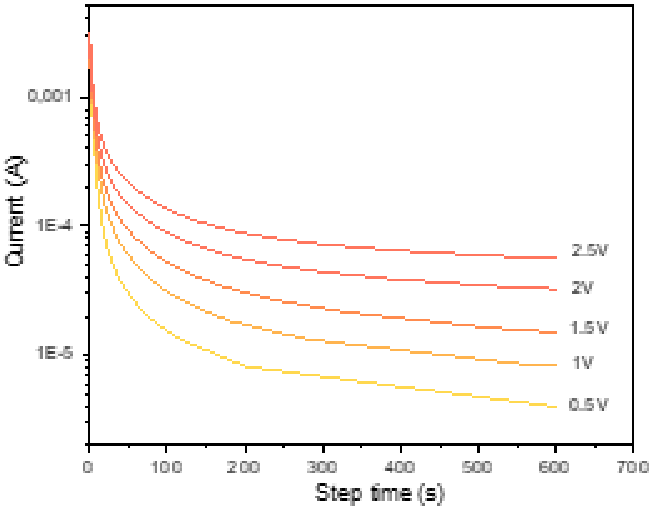

Figure 5.7: Voltage dependence of the current during 10 minutes float time for SC containing $[PYR_{14}][TFSI]$ 1M in PC.

Figure 5.8 displays additional plots of leakage current versus voltage. The first plot compares different electrolytes, all with a concentration of 1M in PC. It is noteworthy that the organic salt-based electrolytes exhibit lower $I_{leakage}$ for lower floating voltages, while the ionic liquid displays a smaller value of $I_{leakage}$ for higher voltages. The second plot compares electrolytes based on $[PYR_{14}][TFSI]$ at different concentrations in PC. With an increase in ionic liquid concentration, the leakage current decreases.

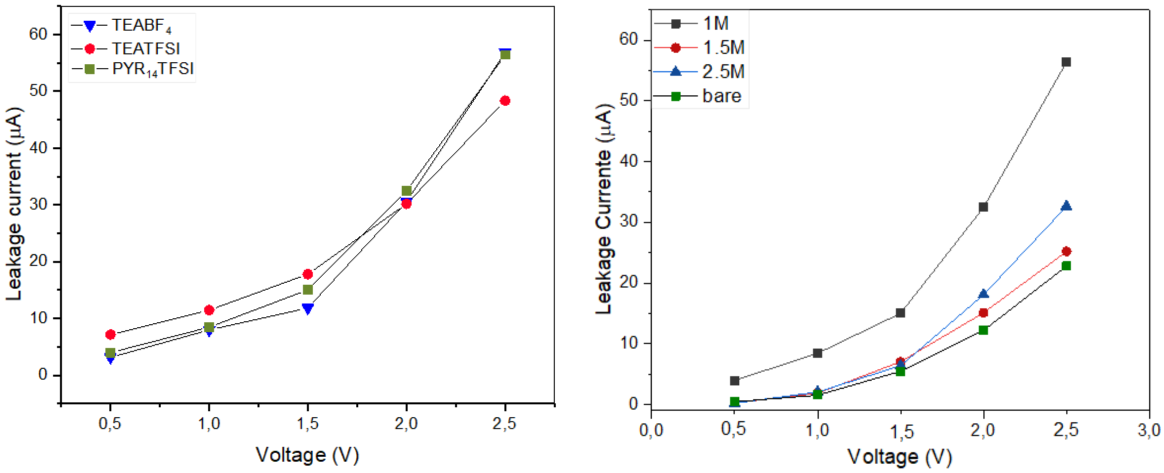

Figure 5.8: Voltage dependence of the leakage current. On the left side different electrolytes 1M in PC are compared. On the right side electrolytes based on $[PYR_{14}][TFSI]$ at different concentrations in PC are compared.

The dependence of the open circuit voltage (OCV) on the initial voltage is emphasized in figure 5.9. A faster decrease of the voltage during the open circuit condition higher initial voltages.

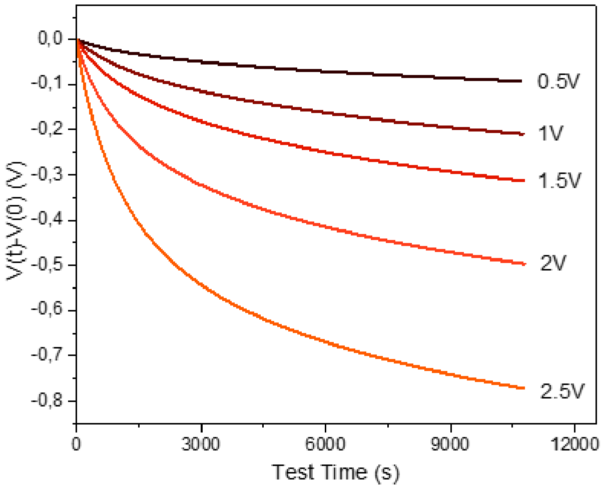

Figure 5.9: Open circuit voltage over a period of three hours for SC containing $[PYR_{14}][TFSI]$ 1M in PC.

Figure 5.10 displays additional plots of OCV for different initial voltages (1V and 2V). It compares different electrolytes, all with a concentration of 1M in PC. The phenomenon of self-discharge has a greater impact on the ionic liquid-based SC.

Figure 5.11 compares the OCV of SCs with different concentrations of $[PYR_{14}][TFSI]$ in PC. At a lower initial voltage (V(0)=1V), the SCs with more concentrated ionic liquid show less self-discharge impact. For higher V(0), the SC comprising $[PYR_{14}][TFSI]$ 1M in PC shows a lower self-discharge compared to higher concentrated electrolytes, yet still higher compared to the bare ionic liquid case.

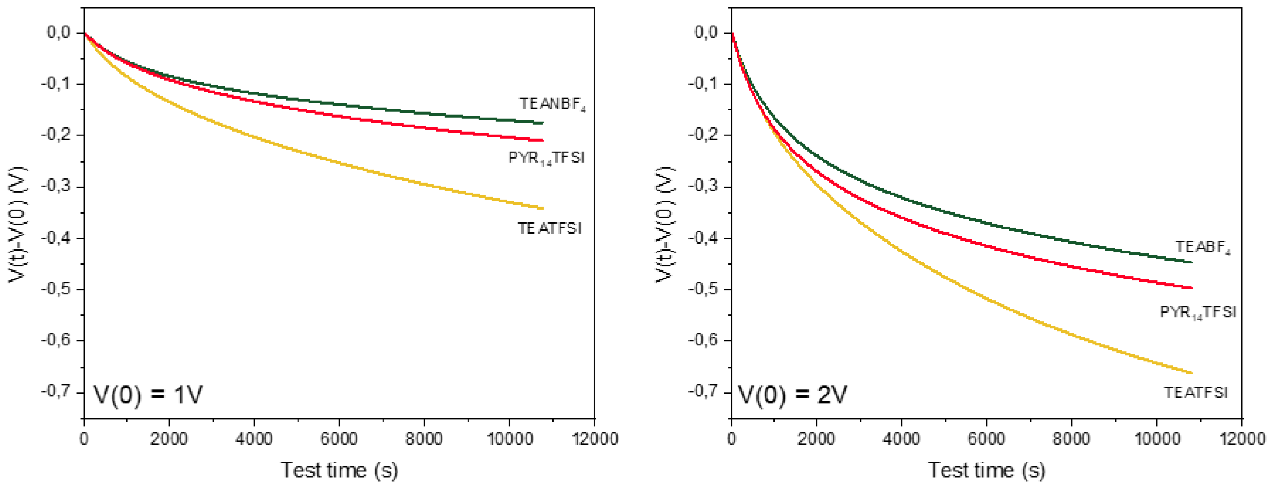

Figure 5.10: Open circuit voltage for different V(0) and for different electrolytes 1M in PC.

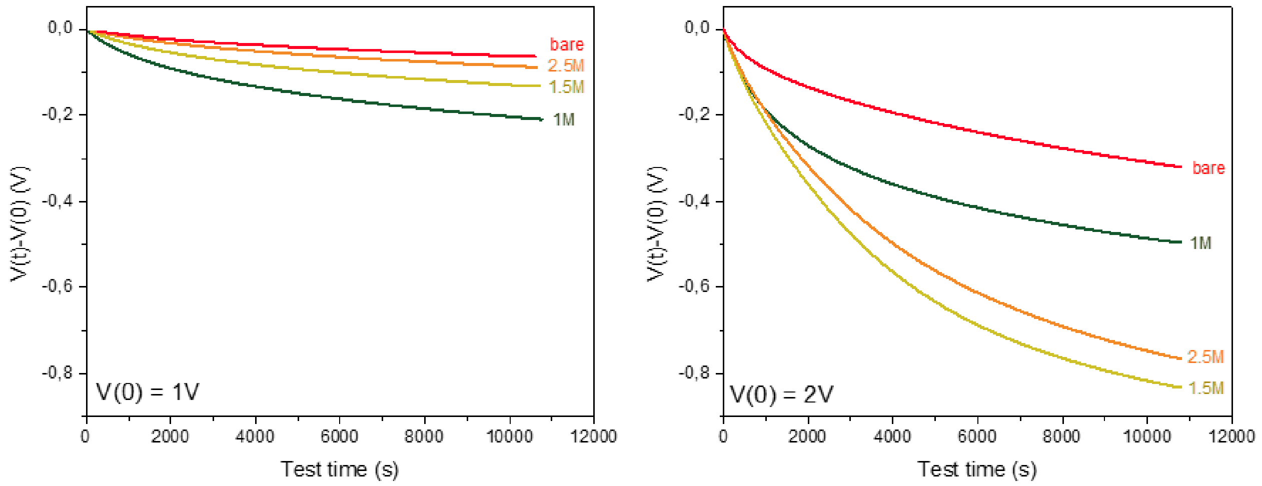

Figure 5.11: Open circuit voltage for SCs with different concentrations of [PYR$_{14}$][TFSI] in PC.

A crucial result of this initial analysis was to verify the correct behavior of the supercapacitors and to set limits for safe operating conditions, especially with regard to the applied voltages, in order to limit losses and avoid device degradation. The safety potential window can be established using various techniques, such as cyclic voltammetry. In this scenario, the electrochemical stability of the system was prioritized as the device is a symmetrical system in terms of the mass of electrodes and active materials. The self-discharge phenomenon is very strong when higher voltages are applied. Furthermore, this phenomenon is highly temperature dependent, in particular, the higher the temperature, the greater the impact of the self-discharge (and also of the leakage current) [31]. Since the SC in this study is expected to operate in a thermocapacitive cycle, it was decided to set the safe potential window from 0V to 2V to limit the effect of the self discharge at higher temperature.

Subsequently, another setup was tested: the assembled supercapacitors in the pouch cell configuration were characterized using electrochemical characterization techniques, mainly cyclic voltammetry (CV) and electrochemical impedance spectroscopy (EIS). The resulting data were used to calculate several figures of merit, specifically the specific capacitance, equivalent series resistance (ESR), coulombic efficiency and energy efficiency. The measurements were carried out in a two-electrode configuration. For all the CVs, a scan rate of 5mVs^{-1} was chosen and 50 cycles were performed. The potential windows examined ranged from 0 V to 0.5 V and up to 2 V with 0.5 V increments. Three supercapacitors containing different electrolytes were analyzed. The electrolytes used are [PYR$_{14}$][TFSI], TEABF$_4$, TEATFSI 1M in PC. Figure 5.12 shows the last cycle of each series of measurements for each SC. It is evident that as the voltage window increases, so does the capacitance. However, simultaneously, the curve deviates slightly from the ideal rectangular shape and the horn-like shape appears in the higher voltage regions. From the CV measurements specific capacitance, coulombic and energy efficiencies can be computed.

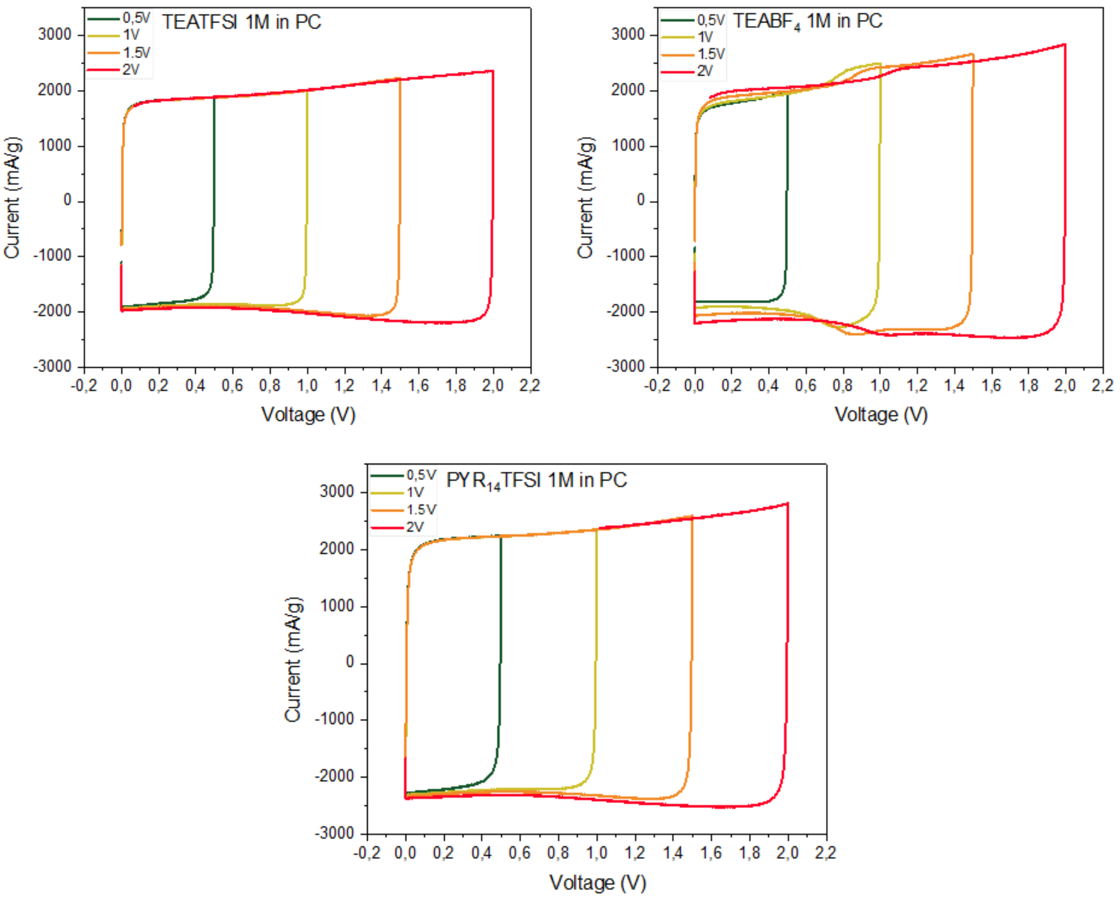

Figure 5.12: Last CV cycle at 5mV/s for SCs containing [PYR$_{14}$][TFSI], TEABF$_4$, TEATFSI 1M in PC.

In addition, electrochemical impedance spectroscopy (EIS) was performed before and after each set of CVs. The frequency range studied was from 10 mHz to 1 MHz, with 10 points per decade. The Nyquist plots related to the final EISs for the three SCs are shown in Figure 5.13. From these plots, the SCs ESRs can be calculated, which are associated with the resistivity of electrodes, bulk electrolyte, and contacts. Furthermore, the Nyquist plot provides information regarding the capacitance and the resistance associated with ions diffusion.

All values of the parameters discussed above and extracted from the previous electrochemical characterizations are reported in the table below (Table 5.2). The voltage dependency of these parameters is emphasized in figure 5.14.

The data reveals that the SC composed of $TEABF_4$ has the smallest ESR value. The SC based on [PYR14][TFSI] has overall the highest specific capacitance values for each applied voltage.

In general coulombic efficiencies are above 99.5%, which is quite high. This refers to the ability of the device to release all of the stored charge after the charging process. Also, the energy efficiencies are high (above 90%) and it can be observed that they increase as the voltage rises. Specific capacitances and energy efficiencies are higher for this configuration compared to the pouch cell configuration. This is may be due to higher losses for the coin cell setup.

Table 5.2: Specific capacitance, coulombic and energy efficiencies, ESR voltage dependency for SCs containing $[PYR_{14}][TFSI]$, $TEABF_4$ and TEATFSI 1M in PC

Electrolytes	Voltage (V)	Specific Capacitance (Fg^{-1})	Coulombic Efficiency (%)	Energy Efficiency (%)	ESR (Ohm)
$[PYR_{14}][TFSI]$	0.5	19.959339	99.961096	91.502017	1.0179
	1	20.667516	99.952007	94.370843	
	1.5	21.490054	99.973550	95.625244	
	2	22.467160	99.954514	95.739863	
$TEABF_4$	0.5	16.749275	99.986945	93.852653	0.7642
	1	18.939199	99.817171	94.497565	
	1.5	20.547673	99.565203	94.501489	
	2	21.602116	99.538126	94.780251	
TEATFSI	0.5	16.902840	99.975932	93.537509	0.9226
	1	17.510446	99.975860	95.595715	
	1.5	18.309302	99.980230	96.474834	
	2	19.128509	99.939162	96.677815	

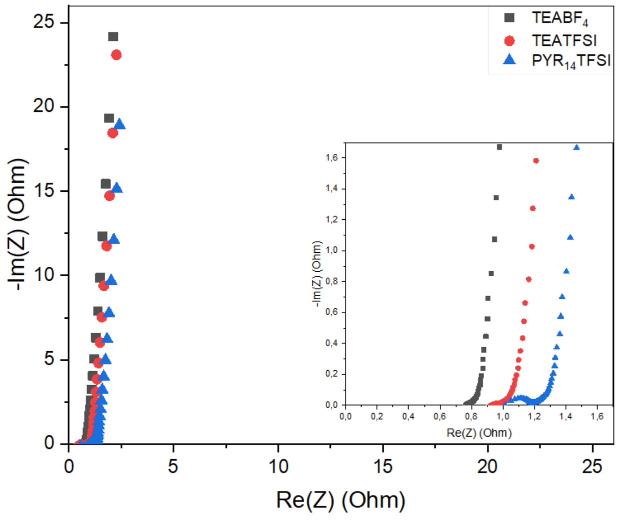

Figure 5.13: Nyquist plot from electrochemical impedance spectroscopy (EIS) for SCs containing $[PYR_{14}][TFSI]$, $TEABF_4$, TEATFSI 1M in PC.

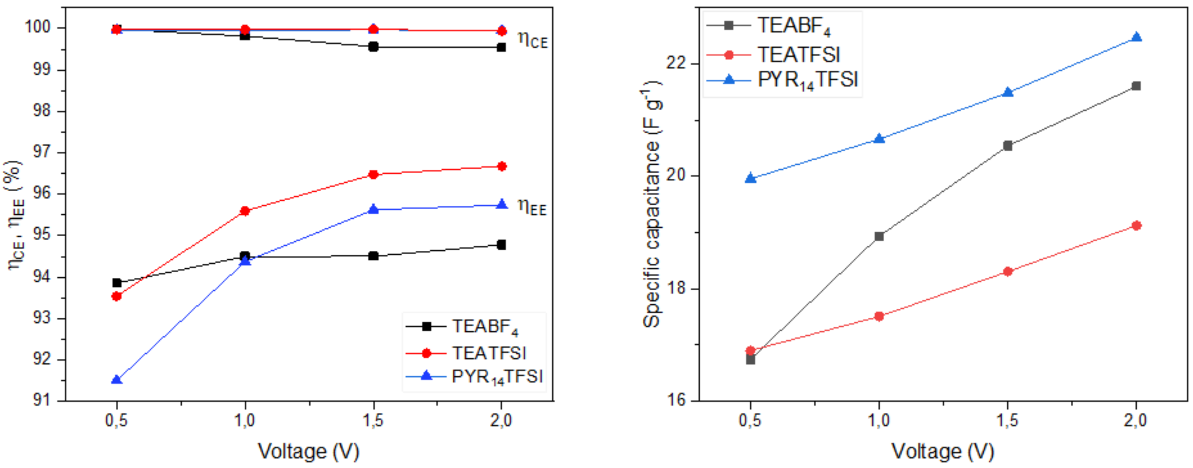

Figure 5.14: Specific capacitance, coulombic and energy efficiencies voltage dependency for SCs containing $[PYR_{14}][TFSI]$, $TEABF_4$ and TEATFSI 1M in PC.

5.3 EDLC thermal energy harvesting

After conducting electrochemical analysis on the SCs, the SCs were used to perform a thermocapacitive cycle for thermal energy harvesting. Initially, the impact of temperature on the ESR was studied by performing EISs at different temperatures. While capacitance has only a very weak dependence on temperature, the ESR decreases considerably with an increase in temperature [32]. Figure 5.15 shows the EIS dependence on temperature. For this purpose a coin cell containing [PYR14][TFSI] 1M in PC was used. It was observed that the width of the semicircle decreased as the temperature increased, indicating a reduction in the interfacial impedance between the electrode and bulk electrolyte [33].

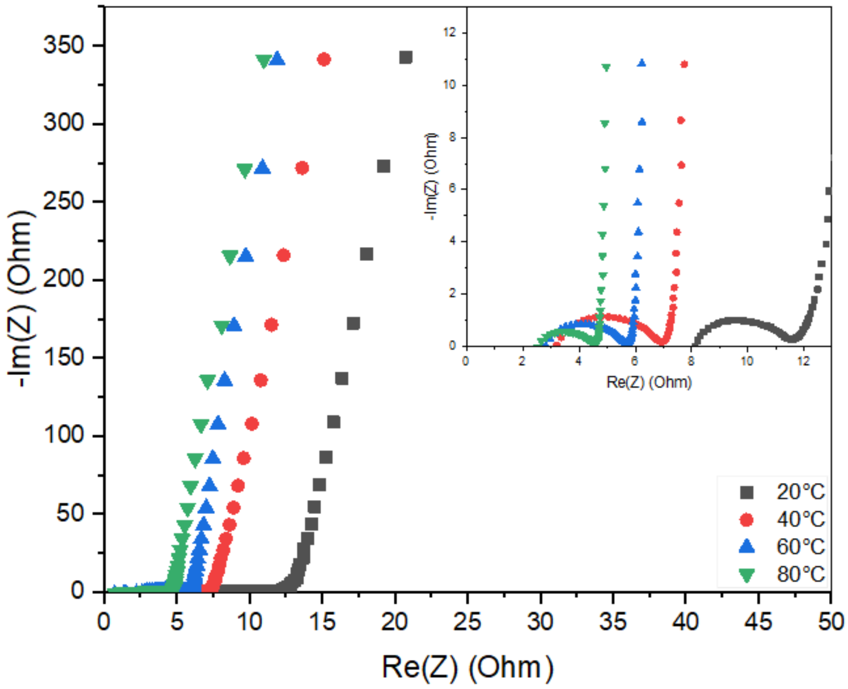

Figure 5.15: EIS experiments carried out at temperatures of 20°C, 40°C, 60°C, and 80°C employing a coin cell comprising [PYR14][TFSI] 1M in PC.

Procedure

The procedure employed in this work is inspired by that proposed in the work of Hartel et al. [19] discussed in Section 3.4. The steps involved in the procedure used in this work are as follows and are shown in the sketch in Figure 5.16:

1. Constant current: a constant current of 5mA was employed to charge the SC until a specified voltage is attained. Throughout this step, the SC was maintained in a low-temperature (T_{low}) environment, which consisted of a constant-temperature cold bath made up of a mixture of ice and water;
2. Constant voltage: a constant voltage is applied to the SC for ten minutes. Also in this step, the SC is kept at T_{low};
3. Open circuit Voltage: after the charging time of the previous steps, the SC is moved into a constant-temperature (T_{high}) hot bath in open circuit mode. A thermal voltage rise is observed and the cell voltage reaches its maximum value;

4. Constant current: when the thermal voltage rise reaches its maximum value, the SC is discharged at a constant current of -5mA until the SC voltage reaches 0V. During this step, the SC once again placed in the cold bath with a constant-temperature T_{low}.

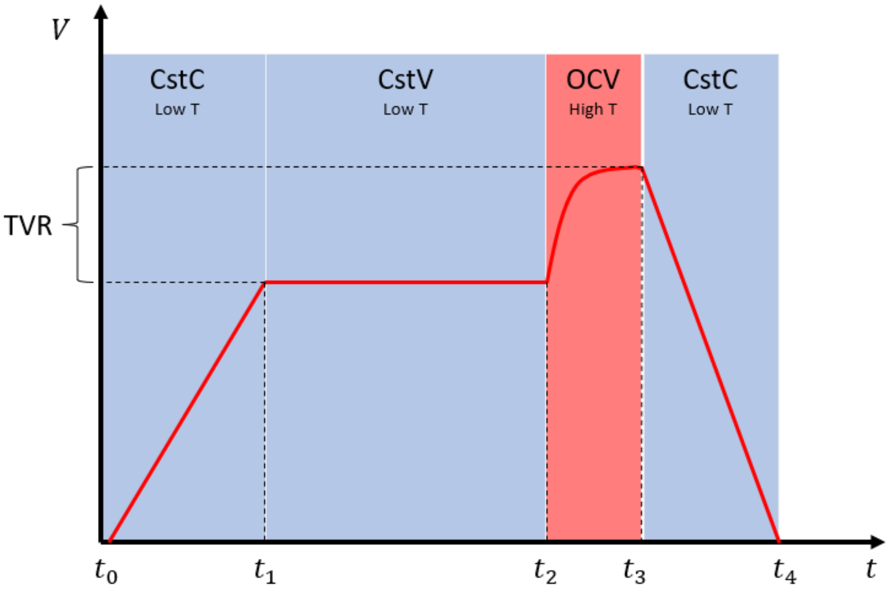

Figure 5.16: Sketch of the procedure adopted in this work.

Different setups of supercapacitors were tested, which included coin cell and pouch cell.

Coin Cell

Supercapacitors with different electrolytes were used. The SCs were tested with different applied voltages: 1V,1.5V and 2V. For each group of measurements, the procedure was performed three times and the mean of the TVR was computed.

Initially, coin cells with different concentrations of [PYR14][TFSI] in PC were tested, with a temperature gradient of 80°C. Figure 5.17 illustrates the TVR as a function of the voltage applied to the SCs and the concentration of [PYR14][TFSI] in PC. The 1.5 M and pure ionic liquid cases exhibited no TVR at all. The highest value was shown for the 1M case with 2V applied.

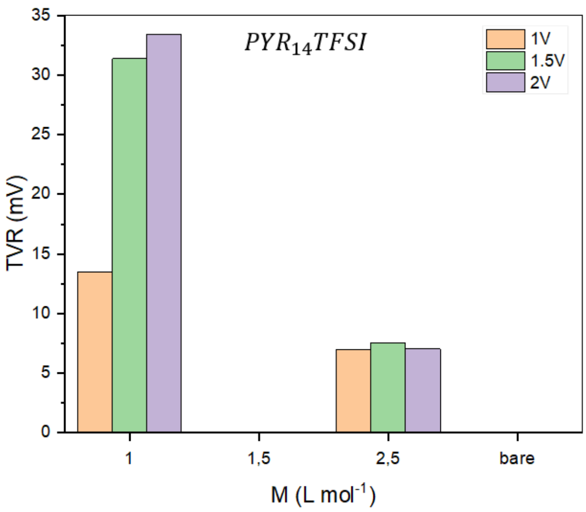

Figure 5.17: TVRs for a coin cell consisting of [PYR14][TFSI] 1M in PC as a function of the ionic liquid concentration and voltage applied. The temperature gradient studied was 80°C.

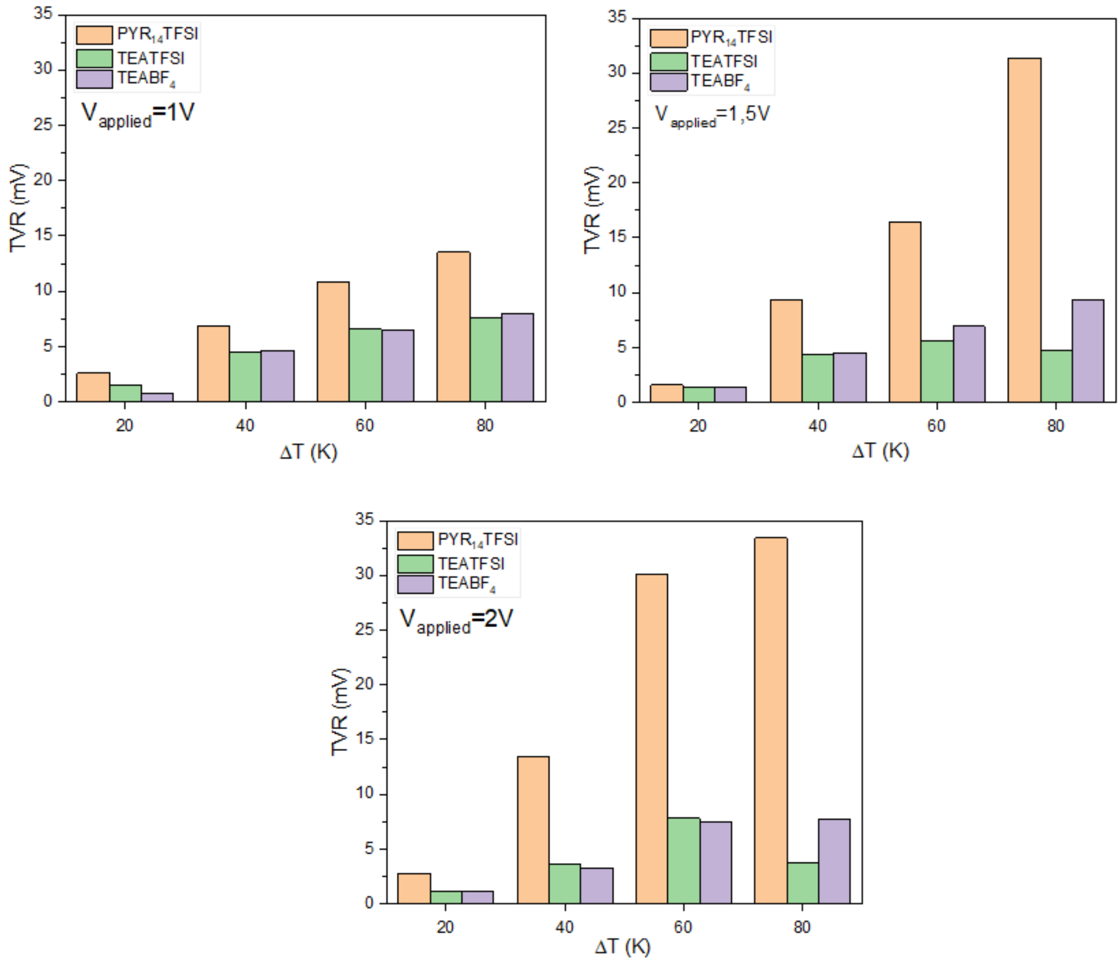

Figure 5.18: TVRs for coin cells consisting of [PYR14][TFSI] 1M in PC, TEABF4 1M in PC, TEATFSI 1M in PC as a function of different voltages applied and different temperature gradients.

Subsequently coin cells with TEABF$_4$ 1M in PC, TEATFSI 1M in PC, [PYR14][TFSI] 1M in PC were tested. Four temperature gradients were analyzed: 20°C, 40°C, 60°C, 80°C. Three different voltages applied were considered: 1V, 1.5V, 2V. The resulting TVR are reported in figure 5.18. Figure 5.18 reveals that the [PYR14][TFSI] case exhibits the highest values of TVRs which are proportional to the applied voltage and the temperature gradient.

Pouch Cell

The same measurements were carried out with pouch cells (previously characterized) containing identical electrolytes. Figure 5.19 presents the measured TVRs.

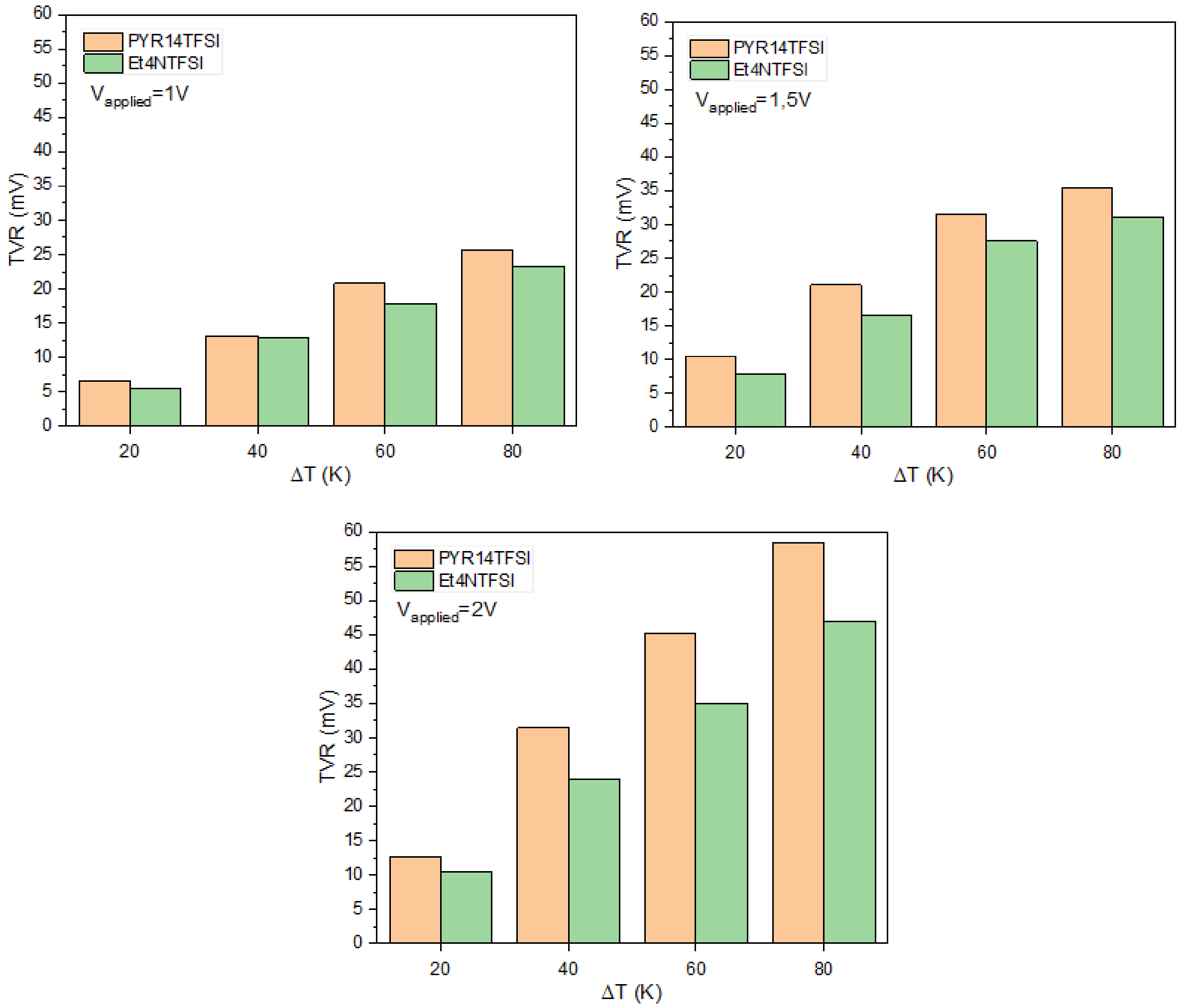

Figure 5.19: TVR for coin cells consisting of [PYR$_{14}$][TFSI] 1M in PC and TEATFSI 1M in PC as a function of different voltages applied and different temperature gradients.

The results showed the same trend as the coin cell case, but the overall TVRs are higher with this setup. Notably, the SC containing [PYR$_{14}$][TFSI] 1M in PC and subjected to a voltage applied of 2V has the highest TVR value of 58.425 mV.

Chapter 6

Conclusions and future developments

There is a positive correlation between the activation energy and the curves slope on the Walden plot, as discussed in Chapter 5. Accordingly, a similar slope for the electrolytes implies that all of them have a similar activation energy for ionic transport. The table that follows (Table 6.1) details the slopes determined by a linear fit of the conductivity and viscosity values on the Walden plot for each of the electrolytes analyzed.

Table 6.1: Slope values obtained from linear fit of the conductivity and viscosity values on the Walden plot for different electrolytes.

Electrolytes	Slope
[PYR_{14}][TFSI] 1M in PC	1,04447
[PYR_{14}][TFSI] 1.5M in PC	0,98548
[PYR_{14}][TFSI] 2.5M in PC	1,00988
[PYR_{14}][TFSI] bare	1,98447
TEATFSI	1,07345
$TEABF_4$	1,05956

In figure 6.1 are reported the TVR vs temperature for pouch cell SCs consisting of [PYR14][TFSI] 1M in PC and TEATFSI 1M in PC as a function of different voltages applied and different temperature gradients. In figure 6.2 it is reported the Walden Plot.

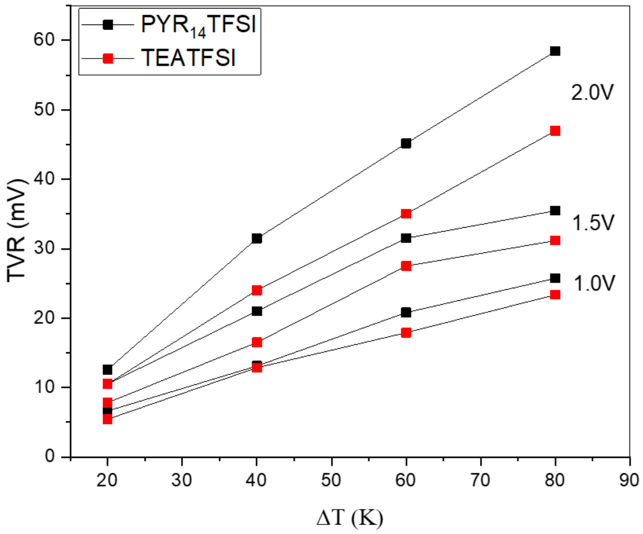

Figure 6.1: TVR vs temperature for pouch cell SCs with [PYR14][TFSI] 1M in PC and TEATFSI 1M in PC as a function voltages applied and temperature gradient.

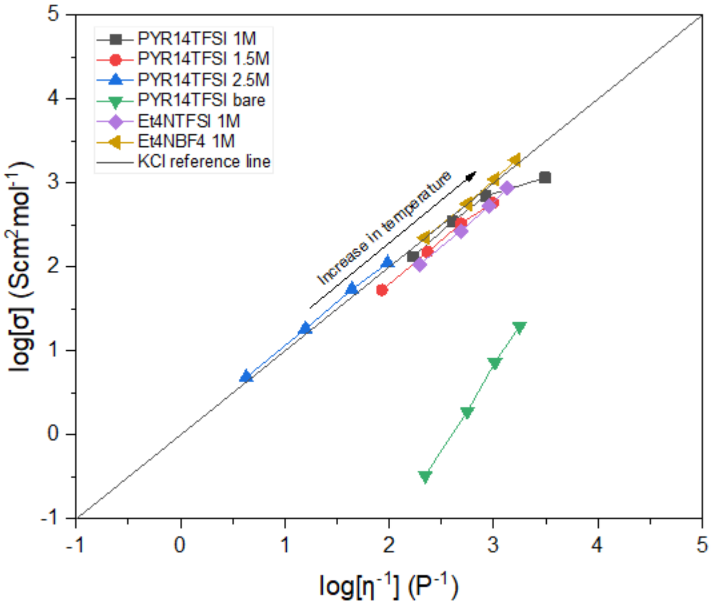

Figure 6.2: Walden plot.

By correlating the TVR with the information gained from the Walden plot, it can be stated that the activation energy plays a fundamental role for the same electrolyte concentration cases. According to the table above, the [PYR$_{14}$][TFSI] 1M in PC has a lower slope than the TEATFSI 1M in PC and is closer to the KCl reference line. This means that TEATFSI 1M in PC has a lower ionicity and the phenomenon of ionic association may be more significant compared to the [PYR$_{14}$][TFSI] 1M in PC. It should be noted that only a comparison is made for the 1M electrolytes case. Additionally, data on TVR vs temperature are required also for TEABF$_4$.

Furthermore, with regard to the difference in slope on the TVR vs T plot (only coin cell setup was considered), according to the potentials theory in concentration cells, variations in species concentration can cause a chemical potential variation since activity is varying. These potentials and potential differences can be described in a Nernstian way:

$$\pi = \frac{RT}{zF} \ln (Q)$$

where R is the gas constant, T is the temperature, z is the ion valency, F is the Faraday constant, and Q is the ration between the ion's activities. Since the value of z remains constant for all salts and temperature variations, the difference in the slope can only be caused by variations in concentration. This leads to a difference in the population of the EDL at different temperatures, so probably different ionicities.

In addition, by recalling the Coulomb interaction:

$$\mathrm{F} = \frac{1}{4\pi\varepsilon_0\varepsilon_r}\frac{q_1 q_2}{r^2}$$

It can be noted that association is promoted if valences are high, distances are high, and dielectric constants are low. Propylene Carbonate provides a high dielectric constant (about 61) thus it screens ions better than the ionic liquid itself (on average, ionic liquid's alkyl chains possess around 10 relative permittivity or so). Moreover, diluting increases the average ion-ion distance reducing the probability of association. Therefore low concentration dilutions of [PYR14][TFSI] in PC should be explored and add to this dissertation.

Concerning the higher concentration of [PYR14][TFSI] in PC, the 2.5M case shows superionicity but a lower conductivity compared to the 1M case. Additionally, the self-discharge results indicate worse behavior compared to the 1M case. Eventually, further measurements are necessary to evaluate self-discharge and leakage current at different temperatures.

Based on the results obtained from the thermocapacitive cycle using the fabricated pouch cell supercapacitors, the supercapacitor containing [PYR14][TFSI] 1M in PC exhibited the best performance. When subjected to a 2V applied voltage, it exhibited a TVR value of 58.425 mV, the highest of all measurements. Notably, it shows a thermal voltage rise of 0.73 mV/K over a temperature window of 0°C to 80°C when a voltage of 2V is applied to the supercapacitor. Figure 6.3 shows a comparison of the TVR slope values (in mV/K) obtained through linear interpolating the values of the TVR vs temperature plot, for SCs containing [PYR14][TFSI] 1M in PC and TEATFSI 1M in PC. The comparison is shown over a temperature window from 0°C to 80°C as a function of the voltage applied to the cell.

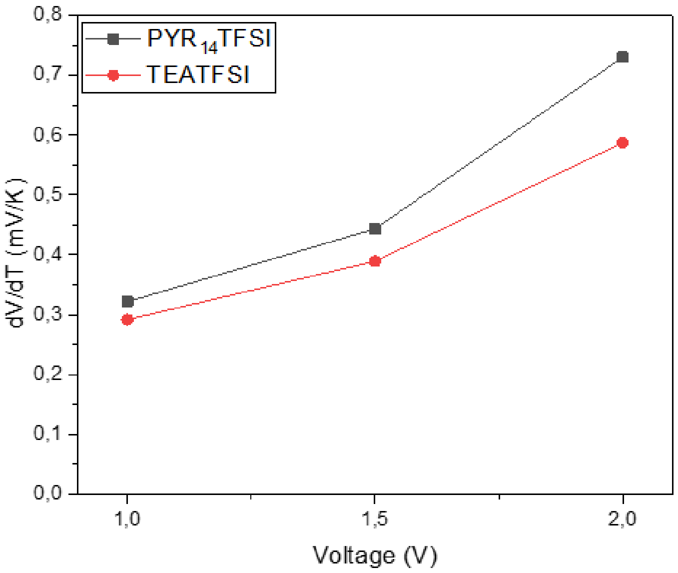

Figure 6.3: TVR slopes comparison of supercapacitors with [PYR14][TFSI] 1M in PC and TEATFSI 1M in PC over a temperature window from 0°C to 80°C as a function of the voltage applied to the cell.

Bibliography

[1] IPCC, 2021: Summary for Policymakers. In: Climate Change 2021: The Physical Science Basis. Contribution of Working Group I to the Sixth Assessment Report of the Intergovernmental Panel on Climate Change [Masson-Delmotte, V., P. Zhai, A. Pirani, S.L. Connors, C. Péan, S. Berger, N. Caud, Y. Chen, L. Goldfarb, M.I. Gomis, M. Huang, K. Leitzell, E. Lonnoy, J.B.R. Matthews, T.K. Maycock, T. Waterfield, O. Yelekçi, R. Yu, and B. Zhou (eds.)]. In Press. (cit. on p. 4).

[2] The Paris Agreement, url: https://unfccc.int/sites/default/files/resource/parisagreement_publication.pdf (cit. on p. 4).

[3] IPCC, 2022: Summary for Policymakers [P.R. Shukla, J. Skea, A. Reisinger, R. Slade, R. Fradera, M. Pathak, A. Al Khourdajie, M. Belkacemi, R. van Diemen, A. Hasija, G. Lisboa, S. Luz, J. Malley, D. McCollum, S. Some, P. Vyas, (eds.)]. In: Climate Change 2022: Mitigation of Climate Change. Contribution of Working Group III to the Sixth Assessment Report of the Intergovernmental Panel on Climate Change [P.R. Shukla, J. Skea, R. Slade, A. Al Khourdajie, R. van Diemen, D. McCollum, M. Pathak, S. Some, P. Vyas, R. Fradera, M. Belkacemi, A. Hasija, G. Lisboa, S. Luz, J. Malley, (eds.)]. Cambridge University Press, Cambridge, UK and New York, NY, USA. DOI: 10.1017/9781009157926.001. (cit. on p. 7).

[4] Dhakal, S., J.C. Minx, F.L. Toth, A. Abdel-Aziz, M.J. Figueroa Meza, K. Hubacek, I.G.C. Jonckheere, Yong-Gun Kim, G.F. Nemet, S. Pachauri, X.C. Tan, T. Wiedmann, 2022: Emissions Trends and Drivers. In IPCC, 2022: Climate Change 2022: Mitigation of Climate Change. Contribution of Working Group III to the Sixth Assessment Report of the Intergovernmental Panel on Climate Change [P.R. Shukla, J. Skea, R. Slade, A. Al Khourdajie, R. van Diemen, D. McCollum, M. Pathak, S. Some, P. Vyas, R. Fradera, M. Belkacemi, A. Hasija, G. Lisboa, S. Luz, J. Malley, (eds.)]. Cambridge University Press, Cambridge, UK and New York, NY, USA. DOI: 10.1017/9781009157926.004. (cit. on p. 238).

[5] IEA, World total energy supply by source, 1971-2019, IEA, Paris https://www.iea.org/data-and-statistics/charts/world-total-energy-supply-by-source-1971-2019 , IEA. License: CC BY 4.0

[6] url: https://www.e3s-conferences.org/articles/e3sconf/abs/2019/39/e3sconf_supehr18_03010/e3sconf_supehr18_03010.html .

[7] Forman, C., Muritala, I. K., Pardemann, R., & Meyer, B. (2016). Estimating the global waste heat potential. In Renewable and Sustainable Energy Reviews (Vol. 57, pp. 1568–1579). Elsevier Ltd. https://doi.org/10.1016/j.rser.2015.12.192

[8] Hur, S., Kim, S., Kim, H. S., Kumar, A., Kwon, C., Shin, J., Kang, H., Sung, T. H., Ryu, J., Baik, J. M., & Song, H. C. (2023). Low-grade waste heat recovery scenarios: Pyroelectric, thermomagnetic, and thermogalvanic thermal energy harvesting. Nano Energy, 114. https://doi.org/10.1016/j.nanoen.2023.108596 .

[9] Firth, A., Zhang, B., & Yang, A. (2019). Quantification of global waste heat and its environmental effects. Applied Energy, 235, 1314–1334. https://doi.org/10.1016/j.apenergy.2018.10.102

[10] Kishore, R. A., & Priya, S. (2018). A Review on low-grade thermal energy harvesting: Materials, methods and devices. In Materials (Vol. 11, Issue 8). MDPI AG. https://doi.org/10.3390/ma11081433 (cit. on p. 3).

[11] Brogioli, D., & la Mantia, F. (2021). Innovative technologies for energy production from low temperature heat sources: Critical literature review and thermodynamic analysis. In Energy and

Environmental Science (Vol. 14, Issue 3, pp. 1057–1082). Royal Society of Chemistry. https://doi.org/10.1039/d0ee02795b. (cit on p. 9).

[12] Al-Zubaidi, A., Ji, X., & Yu, J. (2017). Thermal charging of supercapacitors: A perspective. In Sustainable Energy and Fuels (Vol. 1, Issue 7, pp. 1457–1474). Royal Society of Chemistry. https://doi.org/10.1039/c7se00239d. (cit. on p. 3)

[13] S. W. Lee, Y. Yang, H.-W. Lee, H. Ghasemi, D. Kraemer, G. Chen, Y. Cui, An electrochemical system for efficiently harvesting low-grade heat energy, Nature Communications 5 (2014) 3942. DOI:10.1038/ncomms4942 .

[14] Y. Yang, J. Loomis, H. Ghasemi, S. W. Lee, Y. J. Wang, Y. Cui, G. Chen, Membrane-free battery for harvesting low-grade thermal energy, Nano Lett. 14 (2014) 6578. DOI:10.1021/nl5032106.

[15] Shalini Kulandaivalu and Yusran Sulaiman. «Recent advances in layer-bylayer assembled conducting polymer based composites for supercapacitors». In: Energies 12 (11 2019). ISSN: 19961073. DOI:10.3390/en12112107.

[16] D. Tashima, K. Kurosawatsu, M. Otsubo and C. Honda, "Relation between Space Charge and Pore Size of Nano Porous Electrode for Super Capacitor," 2006 IEEE Conference on Electrical Insulation and Dielectric Phenomena, Kansas City, MO, USA, 2006, pp. 125-128, DOI: 10.1109/CEIDP.2006.312077.

[17] Sharma, S., & Chand, P. (2023). Supercapacitor and electrochemical techniques: A brief review. In Results in Chemistry (Vol. 5). Elsevier B.V. https://doi.org/10.1016/j.rechem.2023.100885

[18] Zhong, C., Deng, Y., Hu, W., Qiao, J., Zhang, L., & Zhang, J. (2015). A review of electrolyte materials and compositions for electrochemical supercapacitors. In Chemical Society Reviews (Vol. 44, Issue 21, pp. 7484–7539). Royal Society of Chemistry. https://doi.org/10.1039/c5cs00303b

[19] Härtel, A., Janssen, M., Weingarth, D., Presser, V., & van Roij, R. (2015). Heat-to-current conversion of low-grade heat from a thermocapacitive cycle by supercapacitors. Energy and Environmental Science, 8(8), 2396–2401. https://doi.org/10.1039/c5ee01192b

[20] B. E. Conway. «Treatments of Impedance Behavior of Various Circuits and Modeling of Double-Layer Capacitor Frequency Response». In: Electrochemical Supercapacitors: Scientific Fundamentals and Technological Applications. Boston, MA: Springer US, 1999, pp. 525–556. ISBN: 978-1-4757-3058-6. DOI: 10.1007/978-1-4757-3058-6_17. url: https://doi.org/10.1007/978-1-4757-3058-6_17 (cit. on pp. 16, 17, 23) .

[21] Harris, A. R., Molino, P. J., Kapsa, R. M. I., Clark, G. M., Paolini, A. G., & Wallace, G. G. (2015). Correlation of the impedance and effective electrode area of doped PEDOT modified electrodes for brain-machine interfaces. Analyst, 140(9), 3164–3174. https://doi.org/10.1039/c4an02362e

[22] «ConductivityDatasheet». In: (). URL: https://www.amelchem.com/wpcontent/uploads/2020/01/Conductivity_Datasheet.pdf (cit. on p. 27) .

[23] MCR 302e, url: https://wiki.anton-paar.com/it-it/fondamenti-della-reologia/misura-con-reometro/ .

[24] B. Hsia. «Materials Synthesis and Characterization for Micro-supercapacitor Applications». In: PP (Nov. 2013), pp. 1–101. url: https://digitalassets.lib.berkeley.edu/etd/ucb/text/Hsia_ berkeley _0028E _13892.pdf

[25] Dsoke, S., Tian, X., Täubert, C., Schlüter, S., & Wohlfahrt-Mehrens, M. (2013). Strategies to reduce the resistance sources on Electrochemical Double Layer Capacitor electrodes. Journal of Power Sources, 238, 422–429. https://doi.org/10.1016/j.jpowsour.2013.04.031

[26] Pohlmann, S., Kühnel, R. S., Centeno, T. A., & Balducci, A. (2014). The Influence of Anion-Cation Combinations on the Physicochemical Properties of Advanced Electrolytes for Supercapacitors and the Capacitance of Activated Carbons. ChemElectroChem, 1(8), 1301–1311. https://doi.org/10.1002/celc.201402091 .

[27] Zare, M., Ghatee, M. H., & Sami, R. (2019). Assessment of the temperature-dependent viscosity of diverse functionalized ionic liquids: Revisiting the fluidity equation. Fluid Phase Equilibria, 488, 27–39. https://doi.org/10.1016/j.fluid.2019.01.019 .

[28] Schreiner, C., Zugmann, S., Hartl, R., & Gores, H. J. (2010). Fractional walden rule for ionic liquids: Examples from recent measurements and a critique of the so-called ideal KCl line for the walden plot. Journal of Chemical and Engineering Data, 55(5), 1784–1788. https://doi.org/10.1021/je900878j .

[29] Wang, Y., Chen, W., Zhao, Q., Jin, G., Xue, Z., Wang, Y., & Mu, T. (2020). Ionicity of deep eutectic solvents by Walden plot and pulsed field gradient nuclear magnetic resonance (PFG-NMR). Physical Chemistry Chemical Physics, 22(44), 25760–25768. https://doi.org/10.1039/d0cp01431a .

[30] Kobayashi, Y., Tokishita, S., & Yamamoto, H. (2020). Determination of Hansen Solubility Parameters of Ionic Liquids by Using Walden Plots. Industrial and Engineering Chemistry Research, 59(32), 14217–14223. https://doi.org/10.1021/acs.iecr.0c01947

[31] Kowal, J., Avaroglu, E., Chamekh, F., Šenfelds, A., Thien, T., Wijaya, D., & Sauer, D. U. (2011). Detailed analysis of the self-discharge of supercapacitors. Journal of Power Sources, 196(1), 573–579. https://doi.org/10.1016/j.jpowsour.2009.12.028 .

[32] Kötz, R., Hahn, M., & Gallay, R. (2006). Temperature behavior and impedance fundamentals of supercapacitors. Journal of Power Sources, 154(2), 550–555. https://doi.org/10.1016/j.jpowsour.2005.10.048 .

[33] Yoo, H. D., Jang, J. H., Ryu, J. H., Park, Y., & Oh, S. M. (2014). Impedance analysis of porous carbon electrodes to predict rate capability of electric double-layer capacitors. Journal of Power Sources, 267, 411–420. https://doi.org/10.1016/j.jpowsour.2014.05.058

Acknowledgments

Ringrazio il professor Lamberti per la fiducia riposta in me e l’opportunità di crescita professionale all’interno di questo meraviglioso e stimolante gruppo di ricerca. Un ringraziamento speciale va a Pietro, Davide e Simone per avermi accompagnato nelle attività di laboratorio; per essere stati dei punti di riferimento preziosi ed unici; per essere stati sempre presenti dal punto di vista scientifico e umano.